Biophysical Journal Volume 89 October 2005 2835–2854

# Yeast Kinetochore Microtubule Dynamics Analyzed by High-Resolution Three-Dimensional Microscopy

J. F. Dorn,* K. Jaqaman,* D. R. Rines,† G. S. Jelson,† P. K. Sorger,† and G. Danuser*
*Laboratory for Computational Cell Biology, Department of Cell Biology, The Scripps Research Institute, La Jolla, California 92037;
and †Department of Biology, Massachusetts Institute of Technology, Cambridge, Massachusetts 02139

ABSTRACT We have probed single kinetochore microtubule (k-MT) dynamics in budding yeast in the G1 phase of the cell cycle by automated tracking of a green fluorescent protein tag placed proximal to the centromere on chromosome IV and of a green fluorescent protein tag fused to the spindle pole body protein Spc42p. Our method reliably distinguishes between different dynamics in wild-type and mutant strains and under different experimental conditions. Using our methods we established that in budding yeast, unlike in metazoans, chromosomes make dynamic attachments to microtubules in G1. This makes it possible to interpret measurements of centromere tag dynamics as reflecting k-MT dynamics. We have examined the sensitivity of our assay by studying the effect of temperature, exposure to benomyl, and a tubulin mutation on k-MT dynamics. We have found that lowering the temperature and exposing cells to benomyl attenuate k-MT dynamics in a similar manner. We further observe that, in contrast to previous reports, the mutant *tub2-150* forms k-MTs that depolymerize faster than wild type. Based on these findings, we propose high-resolution light microscopy of centromere dynamics in G1 yeast cells as a sensitive assay for the regulation of single k-MT dynamics.

## INTRODUCTION

Chromosome segregation during cell division is mediated by the binding of kinetochores to microtubules (k-MTs). Kinetochores remain bound to k-MT plus-ends during cycles of polymerization and depolymerization, and the regulation of microtubule (MT) dynamics by kinetochores is thought to play a critical role in force generation. Even the simplest kinetochores, such as those in the budding yeast *Saccharomyces cerevisiae*, contain >60 protein subunits, most of whose functions remain unknown (1). Studies in budding yeast have shown, however, that mutations in kinetochore proteins alter movement during mitosis and prevent accurate disjunction of sister chromatids. Recent phylogenetic analysis suggests that, whereas homologs exist for sequence-specific DNA binding components only in a subset of closely related yeasts, many other subunits have been conserved through evolution (2). Determining how individual proteins in simple and complex kinetochores organize in structures that bind k-MTs and regulate their dynamics is the greatest challenge in the field.

During metaphase in both animal and budding yeast cells, chromosomes exhibit directional instability, moving first one way and then the other. This is a result of the random switching of k-MTs between phases of growth and shrinkage, a phenomenon known as MT dynamic instability (3). The rates of MT growth and shrinkage, and the probabilities associated with switches between these states (catastrophe and rescue frequencies) vary with MT environment and are regulated by a spectrum of MT-associated proteins (4). Data obtained in vitro and in vivo also show that MT polymer dynamics are modulated by the amount of tension applied to the MT end (5). Tension, motor, and nonmotor MT-associated proteins are likely to play important roles in the regulation of k-MT dynamics by kinetochores. During metaphase, paired sister kinetochores establish bipolar attachments in which one kinetochore is bound to k-MTs emanating from one pole and the other kinetochore is bound to k-MTs emanating from the other pole. Bipolar attachment generates sufficient tension on kinetochores to deform substantially the structure of centromeric chromatin (6,7). The combination of chromatin deformation and kinetochore directional instability gives rise to transient sister chromatid separation during metaphase (6). Thus, it seems likely that kinetochores constitute a mechanochemical regulator of k-MT dynamics.

*S. cerevisiae* is an ideal organism in which to study the mechanochemical regulation of k-MT dynamics. Kinetochores and spindles in budding yeast are simple when compared to kinetochores and spindles in other organisms, although nonetheless complex in absolute terms. *S. cerevisiae* kinetochores bind to the plus-end of a single k-MT whose minus end is fixed in the spindle pole body (SPB) (8,9). There is no evidence for treadmilling, and thus the motion of kinetochores relates directly to the properties of plus-ends (10). The 60–70 known *S. cerevisiae* kinetochore proteins assemble into at least 15 multiprotein complexes that then bind in a hierarchical fashion to centromeric (CEN) DNA (1,11,12). Loss-of-function mutations are available in many of these proteins and cause a variety of distinct defects in chromosome segregation including loss of chromosome-MT binding, sustained monopolar attachment, and bipolar attachment without the correct force generation (13). Moreover, in *S. cerevisiae* it is possible to track the movement of fluorescent chromosome tags inserted close to centromeric

---

*Submitted December 21, 2004, and accepted for publication July 1, 2005.*

Address reprint requests to G. Danuser, Tel.: 858-784-7096; Fax: 858-784-7103; E-mail: gdanuser@scripps.edu.

0006-3495/05/10/2835/20 $2.00

doi: 10.1529/biophysj.104.058461

DNA and thereby determine the kinetochore motion in living cells (6,14). Chromosome tags consist of tandem copies of an operator site (TetO) bound to fluorescent repressor (TetR-GFP) and give rise to diffraction-limited spots in fluorescence images. We have previously shown that it is possible to accurately track these spots using automated methods (15, 16). By combining loss-of-function mutations in individual kinetochore proteins with automated chromosome tracking we hope to characterize quantitatively live-cell phenotypes of kinetochore mutations and gain insight into the processes of chromosome-k-MT binding.

Despite the promise of this approach, it remains difficult to relate even well-established phenotypes to specific defects in kinetochore function. One problem is that metaphase and anaphase spindles are complex mechanical systems stabilized by a variety of opposing forces (17), in which even highly specific defects have long-range effects. To address this problem, we hope to understand kinetochore-k-MT attachment first in a simpler setting involving the tethering of *S. cerevisiae* chromosomes to spindles during G1 (18). However, MT-dependent chromosome tethering before the onset of mitosis has remained an issue of some controversy (19). On the one hand, chromosome-SPB tethering in *S. cerevisiae* has been reported to survive treatment with the MT depolymerizing drug nocodazole, arguing against MT-dependent attachment (20). On the other hand, the existence in G1 of 16 microtubules (9,21), the haploid chromosome number, suggests that MTs might indeed be involved in establishing a link between SPB and chromosomes. Moreover, fixed-cell (18) data suggest that nocodazole treatment alters the distribution of kinetochores, which are normally clustered around the SPB in G1. In view of such contradicting reports, we therefore began our study by exploiting the trajectories of chromosome tags relative to SPC42-GFP markers located in the SPB to confirm MT- and kinetochore-dependent chromosome attachment in G1. This was achieved by analyzing the differences of chromosome trajectories between wild-type (WT) and *ndc10-1* mutant cells, which lack a functional kinetochore (22,23), and by showing that chromosome trajectories of cells carrying tubulin mutations or treated with MT-affecting drugs display significantly altered chromosome dynamics. We also argue on theoretical and experimental bases that trajectories of centromere proximal tags serve as a reliable measure of kinetochore position and thus of k-MT dynamics. Subsequently, we used this data and data from a series of experiments with temperature variation to establish that we are able for the first time to probe the dynamics of a single k-MT in yeast with high sensitivity. This provides us now with a powerful readout for dissecting the functional linkages between kinetochore proteins and k-MT dynamics by molecular genetics.

This readout critically relies on the development of algorithms for image analysis and statistical data mining. To reliably distinguish between k-MT dynamics in different mutants and under different conditions, we found that it is necessary to acquire three-dimensional (3D) microscopy images at a high rate; every second, we acquire a stack of 18 z-slices with an exposure time of 20 ms per frame. The short exposure time results in images with low signal/noise ratio (SNR) (of ~6) that decreases even further toward the end of each movie due to photobleaching (Fig. 1). To analyze these data, we have developed a software package that automatically determines tag movements in 3D and associated measurement uncertainties. This task is not straightforward, because the low SNR signals of the two tags frequently overlap (Fig. 1, *C-I–C-III*). Resolving them requires algorithms that can distinguish tags of different intensities at distances shorter than the inverse of the frequency cutoff in the microscope's optical transfer function (15,16,24). Based on statistical tests, we can then separate the quasirandom movement of the chromosome and SPB tags from measurement noise and infer the influence of mutations, drugs, and environmental conditions on k-MT dynamics.

## METHODS

### Cell culture and strains

Yeast strains used in this study were derived from the W303 genetic background, except for the *tub2-150* mutant, which was derived from S288C. Centromere IV localization in WT and mutant strains was determined using the −1.1 Ch IV TetO/TetR-GFP construct described in He et al. (6). SPBs were marked using the SPC42-GFP plasmid integrated at the endogenous locus described in He et al. (6).

Cells were prepared for microscopy as described in Rines et al. (25). In brief, cells were grown overnight at room temperature in SC-minimal media supplemented with 20 $\mu$g/ml of adenine and 2% glucose. For *tub2-150*, 40 $\mu$g/ml of benomyl in dimethylsulfoxide were added to the media for normal cell growth and to rescue the tubulin mutation. All cell cultures were grown to mid-log phase, concentrated by centrifugation (4000 rpm) and resuspended in 0.3–0.5 ml of fresh SC-media. The concentrated cell suspension (2.2 $\mu$l) was spotted onto an agarose-coated microscope slide and sealed with a coverslip before imaging.

Temperature-sensitive mutants were imaged by placing the slide with cells directly onto a stage-mounted, temperature-controlled block as described in Rines et al. (26). The cells were typically shifted to restrictive conditions for 1.5–2 h before imaging. For benomyl-dependent experiments, benomyl was added to *ndc10-1* and WT cell cultures 1–2 h before slide mounting and imaging. To image *tub2-150* without benomyl, the cells were resuspended in benomyl-free SC-media 2 h before starting microscopy. To avoid $\alpha$-factor-dependent MT effects on G1 cells, all G1 chromosome dynamics studies were conducted on asynchronous cultures. G1 cells were identified by their round shape and absence of a bud. To ensure that cells were no longer in telophase, daughter cells from a preceding cell division were imaged at bud emergence in the adjacent mother cell.

### Microscopy

Live cell imaging was performed using a DeltaVision optical sectioning microscope on a Nikon TE200 base with a 100×/1.4 N.A. objective and a Photometrics Cool Snap HQ camera (Applied Precision, Issaquah, WA). Endow GFP longpass filter sets (Chroma Technology, Rockingham, VT; catalog No. 41018) were used as fluorescent filtering elements. A custom-built heated stage and Bioptechs objective lens heater were used to maintain cells at the appropriate temperature during imaging. 3D image stacks were collected with 16–18 optical slices of 64 × 64 pixels and a pixel size in

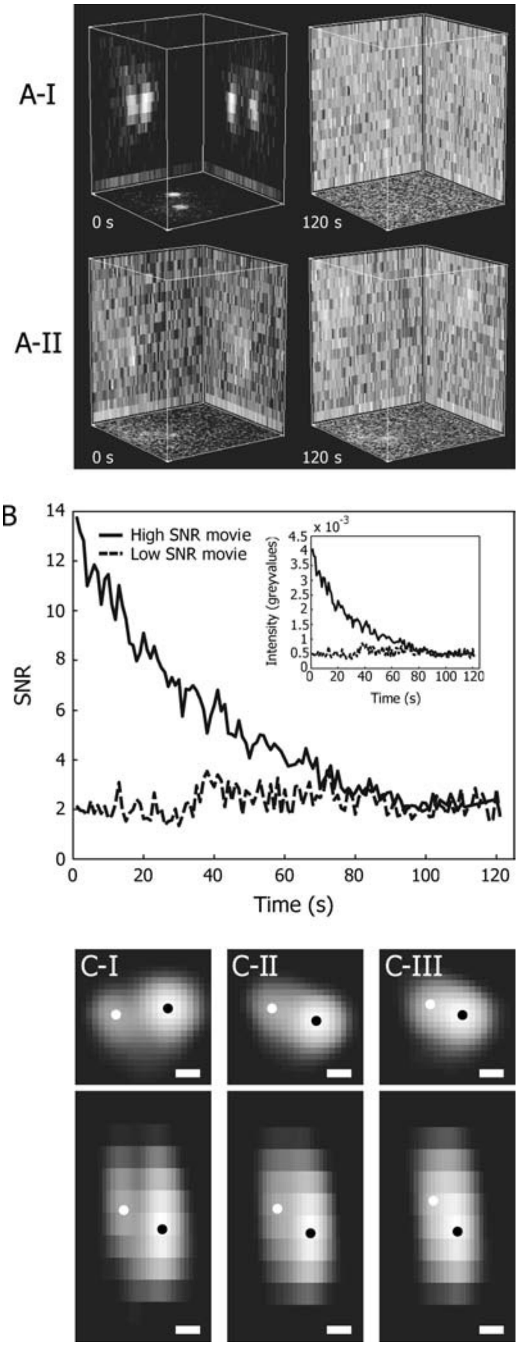

FIGURE 1 3D image stacks of spindle pole body and centromere tag acquired by fast sampling and low light exposure. (*A-I* and *A-II*) 3D maximum projections of the first and the last images in a raw movie with initially high (*A-I*) and low (*A-II*) signal/noise ratio. The size of the stacks is $3 \times 3 \times 4$ $\mu$m. See supplementary movies S1 and S2 for animated image sequences. (*B*) SNR and signal intensities (*inset*) of the brighter of the two tags in the movie shown in panels *A-I* (S1, *solid line*) and *A-II* (S2, *dashed line*). The SNR decreases with the decay in intensity induced by photobleaching. (*C-I–C-III*) Maximum projections of noise-filtered, overlapping tag signals. Although the two tags are clearly separable in the image on the left (*C-I*), their signals frequently overlap (*C-II*), and become indistinguishable by visual inspection (*C-III*). Black and white dots, positions of SPB and CEN tag, respectively, as determined by 3D high-resolution microscopy. Bar, 200 nm.

object-space coordinates of 48 nm. The slices were separated by 0.20 ± 0.01 or 0.25 ± 0.01 $\mu$m. Exposure time for each slice was 0.035 s. A frame (i.e., the 16–18 slices) was recorded every 1 or 5 s for a total of 121 time points and compiled computationally using MATLAB (MathWorks, Natick, MA) to generate 3D movie reconstructions. At the beginning and end of each movie, five additional frames were acquired with closed camera shutter for dark frame subtraction as a way to correct for charge-coupled device chip dependent effects. All image processing and data analysis was done using MATLAB.

## Algorithms for detection and tracking of CEN and SPB tags

We define a tag as a fluorophore cluster in the object domain, and a spot as the image of one tag or the overlapping images of several tags. Because the physical size of our tag is below the diffraction limit of the microscope's objective lens, tag signals are point-spread functions (PSFs). The extension of the PSF main lobe is proportional to the inverse of the cutoff frequency of the microscope's optical transfer function (OTF). For the optical setup used in this study the inverses of the frequency cutoffs are 229 nm laterally and 814 nm axially. As shown in Fig. 1, *C-I–C-III*, the signals of two tags closer than twice the PSF extension in any orientation overlap. Owing to the small size of the yeast nucleus, such overlaps occur frequently. In many cases the tag-to-tag distance even drops below the inverse of the frequency cutoff rendering them visually indistinguishable. However, these tags can still be resolved by algorithms that exploit prior knowledge of the specimen and of the image acquisition to extrapolate information from the high SNR domain of the OTF passband to the low SNR domain and the frequency domain beyond the OTF cutoff (24,27,28). In our application, we exploit the following prior knowledge:

- The image of one tag is represented by the PSF of the microscope.
- A spot is the image of an integer number of tags.
- The number of tags is constant throughout the movie.
- Tag intensity does not change over time except for photobleaching, which can be modeled computationally and compensated.

Notice that the algorithm does not restrict the tracking to a specific number of tags, rendering the schema useful for applications beyond the one discussed in this article. Our algorithm for localizing and tracking CEN and SPB tags from the four-dimensional raw image data involves three steps: i), spot detection and tag localization; ii), tag linking, and iii), tag tracking (Fig. 2).

### Spot detection and tag localization

The spot detection module first distinguishes spots from noise, and then applies a mixture-model fitting (MMF) algorithm to localize one or more tags within these spots. It employs the prior knowledge that the tag images are PSFs, and that the images contain an integer number of tags. An initial estimate of spot positions is obtained by extracting local maxima from each 3D frame filtered by the PSF. To distinguish likely spots from noise, the maxima are classified according to a ''spottiness'' measure calculated from the magnitude and curvature of the 3D intensity distributions of filtered signal at each maximum (15). Next we analyze each spot identified as the image of one tag or a superposition of the images of multiple tags in a mixture model $M$ of the form:

$$M(\mathbf{x},\mathbf{a},b,\mathbf{c},n)=\sum_{\mathrm{i}=1}^{\mathrm{n}} a_{\mathrm{i}} \times psf(\mathbf{x}-\mathbf{c}_{\mathrm{i}})+b.$$

The free parameters in the model are the number $n$ of PSF kernels (i.e., tag images contributing to the spot), their center positions $\mathbf{c}_{\mathrm{i}}=(x_{\mathrm{i}},y_{\mathrm{i}},z_{\mathrm{i}})$, their signal magnitudes $a_{\mathrm{i}}$ (i.e., brightness of the isolated image of tag $i$), and a common background intensity $b$ for all tags. The vector $\mathbf{x}$ denotes the

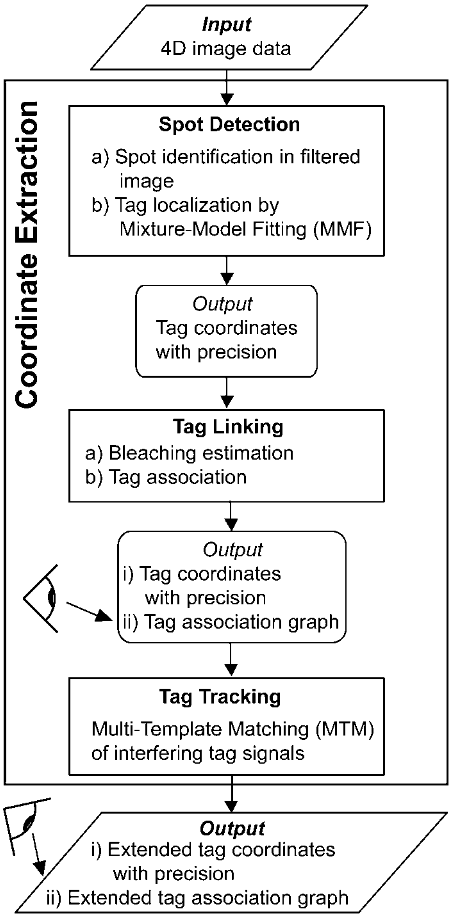

FIGURE 2 Flow chart of the algorithm used to extract tag trajectories from four-dimensional (3D space + time) image data. The spot detection module separates significant spot signals from noise, and applies a mixture-model fitting of multiple point-spread functions to localize one or several tags in each spot. The tag linking module establishes tag correspondence between consecutive frames. The tag tracking module localizes previously unresolved tags by multitemplate matching. Eyes indicate where a graphical user interface allows the user to manipulate otherwise automatically generated data.

position of any voxel inside the volume enclosing the spot analyzed. The main challenge in this kind of parameter estimation is the determination of $n$. We have chosen a bottom-up strategy to identify the optimal balance between degrees of freedom of the model and the $\chi^2$-statistics of residuals between voxel intensities in the raw image data and the fitted model. We start by fitting a model of order $n = 1$. From the intensity residuals, we estimate the uncertainties in signal magnitude and position by means of error propagation (29). If the signal magnitude is not significantly above the image noise, the spot is rejected as a whole. Otherwise, the procedure is repeated for mixture models of increasing order until the improvement of the residual statistics of the model of order $n + 1$ relative to the statistics of the model of order $n$ is not significant, or until the distance between any two kernels is not significant compared to their combined positional uncertainties. Kernels for which any of these tests fail are rejected. The output of the MMF module is a list of tags assigned to each spot, specifying the tags' position and brightness (15). In this step, we also estimate the SNR in the vicinity of each tag, defining it as:

$$SNR_i = a_i/\sigma_b,$$

where $\sigma_b$ is the local noise level, estimated as the square root of the variance of the intensity residuals of the PSF kernel fit $i$ to the raw image. This measure includes contributions from shot noise and camera noise, as well as aberrations of the actual tag image relative to the PSF model. The latter have been shown to be negligible in comparison to the noise level of our faint signals (15).

## *Tag linking*

The tag linking module finds corresponding tags in consecutive frames and stores the relationships in a tag association graph. The algorithm jointly minimizes the overall intensity change (corrected for bleaching) and displacement (corrected for stage drift) of tags between frames while conserving the number of tags (16). When the MMF algorithm has failed to separate all tags in a frame, the linking module assigns multiple tags from the previous frame to the same position, thereby creating a fusion spot. The identification of fusion spots is achieved via superposition rules of tag intensity. The subsequent relative tracking (Step iii) needs the highest possible accuracy. Therefore, we include at this point the possibility for the user to rectify the solution and manually modify false links. On average, <3% of the frames require such manual intervention, as inferred from the analysis of >300 movies. The correction is achieved with a convenient graphical user interface, where the user can reassign links, delete a rare falsely identified spot, or eliminate entire frames. However, we do not allow the user to change tag coordinates or introduce new tags, as we have found that under the low SNR conditions of our 3D data, computer vision based detection and localization are significantly more reliable than position measurements based on visual inference.

## *Tag tracking*

To further enhance the resolution and precision in tag localization, the tag tracking module performs a relative matching of tag signals, exploiting the prior knowledge that tag brightness (corrected for bleaching) is constant over time and that tags do not disappear (16). Tag signals in one frame (source), where tags have been resolved by MMF, are matched to the corresponding signals in a second frame (target) containing several, as yet unresolved, tags (fusion spots). We estimate the tag displacements $\mathbf{d}_k$ between source and target frame by least squares multitemplate matching (MTM) of corresponding tag signals (16). MTM accounts for the overlap of multiple tag signals by first reconstructing overlap-free templates $J_k^S$ in the source, and patches $J_k^T$ in the target frame for all tags $k = 1, \ldots, n$ with image overlap. Patches are constructed by calculating the relative image contribution $r_k(\mathbf{x})$ of tag $k$ to a voxel located inside the image volume of a fusion spot or of a set of spots with signal overlap. We obtain $r_k^S(\mathbf{x})$ and $r_k^T(\mathbf{x})$ by placing PSF kernels in the known and best-guess tag positions in source and target frames, respectively. Tag positions in the target frame are then iteratively updated to match all $n$ overlapping tag signals according to:

$$\hat{\mathbf{d}}_k = \min_{\mathbf{d}_k} \arg \sum_{k=1}^{n} \sum\nolimits_{\forall \text{voxels} \in \text{tag image } k} \left( J_k^S(\mathbf{x}) - J_k^T(\mathbf{x}, \mathbf{d}_k) \right)^2. \quad (1)$$

Importantly, in contrast to MMF, PSF kernels are used only to calculate the relative contributions of a tag to voxels with signal contributions from several tags. This renders the MTM algorithm insensitive to aberrations in the PSF. As long as the aberration is shift invariant over the displacement that is tracked, the contributions $r_k^S(\mathbf{x})$ and $r_k^T(\mathbf{x})$, and thus $J_k^S$ and $J_k^T$, are equally distorted, canceling out in the objective function (Eq. 1). Upon completed matching, the positional uncertainty of every tag localized in the target frame is calculated as the sum of the positional uncertainty of the tag in the source frame and the uncertainty of the MTM displacement estimate. If the distance between tags is significant compared to their combined uncertainties, we update the list of tag coordinates and the tag association graph.

## Calculation of SPB-CEN distance trajectories

In every frame, the SPB-CEN distance is calculated as the magnitude of the 3D vector connecting the two tags. This descriptor of CEN tag motion relative to the SPB tag is both shift and rotation invariant and is designed to represent MT-dependent motion of the CEN tag. The uncertainty in the SPB-CEN distance is calculated from the positional uncertainties of both tags.

## Statistics of mean squared distance changes

Mean squared SPB-CEN distance changes (*MSQDs*) as a function of time lag are calculated as described in Saxton (30), with a maximum time lag of $\tau \leq 0.25T$, where $T$ is the number of time points in the SPB-CEN distance trajectory. The *MSQD* of a set of measurements on the same strain is calculated by averaging *MSQDs* from trajectories of different movies, weighted with their respective uncertainties. At sufficiently long time lags, the *MSQD* of an object undergoing confined motion reaches a plateau (31). This plateau corresponds to the average distance between any two points $\mathbf{r}_1$ and $\mathbf{r}_2$ within the confinement volume $\Omega$:

$$MSQD(\tau \rightarrow \infty) = \int_{\Omega}\int_{\Omega} p(\mathbf{r}_1) \times p(\mathbf{r}_2) \times |\mathbf{r}_2 - \mathbf{r}_1|^2 d\Omega_1 d\Omega_2, \tag{2}$$

where $p(\mathbf{r})$ is the probability that the point $\mathbf{r}$ is visited by the trajectory. If the confined motion corresponds to a random walk, all points in $\Omega$ have an equal probability of being visited, hence $p(r) = 1/\Omega$. For our analysis of chromosome movement, we assume a spherical confinement region of radius $R_C$ centered at (0,0,0), and we place the SPB, our reference point, at $(0,0,R_C)$ on the surface of the confinement region. To prevent external effects such as rotation and translation of the cell or the nucleus from influencing the *MSQD* plateau, we replace the distance vector $\mathbf{r}$ with magnitude of the SPB-CEN distance

$$d_i = \left| \begin{pmatrix} r_i \sin\theta_i \cos\varphi_i \\ r_i \sin\theta_i \sin\varphi_i \\ r_i \cos\theta_i - R_C \end{pmatrix} \right|, i = 1, 2.$$

Equation 2 can thus be rewritten as:

$$MSQD(\tau \rightarrow \infty) = \frac{1}{\left(\frac{4\pi}{3}R_C^3\right)^2} \int_0^{R_C}\int_0^{2\pi}\int_0^{\pi}\int_0^{R_C}\int_0^{2\pi}\int_0^{\pi} |d_2 - d_1|^2 \times r_1^2 r_2^2 \sin\theta_1 \sin\theta_2 d\theta_1 d\varphi_1 dr_1 d\theta_2 d\varphi_2 dr_2,$$

which has an analytical solution of the form:

$$MSQD(\tau \rightarrow \infty) = \frac{8}{25}R_C^2. \tag{3}$$

For a spherical confinement region, $R_c$ can also be calculated from the variance of the SPB-CEN distance trajectory:

$$\sigma^2(d) = E(d^2) - E(d)^2 = \left(\frac{1}{\Omega}\int_{\Omega} d^2 d\Omega\right) - \left(\frac{1}{\Omega}\int_{\Omega} d d\Omega\right)^2 = \frac{4}{25}R_C^2, \tag{4}$$

where $E(\cdot)$ is the expectation value. With Eq. 4, it is possible to estimate the confinement region from data that do not cover enough time to let the *MSQD* curve exhibit the plateau.

## Classification of SPB-CEN distance trajectories

SPB-CEN distance trajectories (Fig. 3 *A*) are divided into periods of antipoleward (AP) motion (*dark gray dashed line*), poleward (TP) motion (*light gray dashed line*), and pause (*light gray dotted line*). Conventionally, MT dynamics are described by first identifying turning points in the directionality of motion. The average time between turning points is used to calculate catastrophe and rescue frequencies. AP and TP speeds are defined as the slope of the line linking the turning points (32). This approach has two major disadvantages: i), it fails to recognize the possibility of heterogeneity in speeds within a period of motion with constant directionality; and ii), in

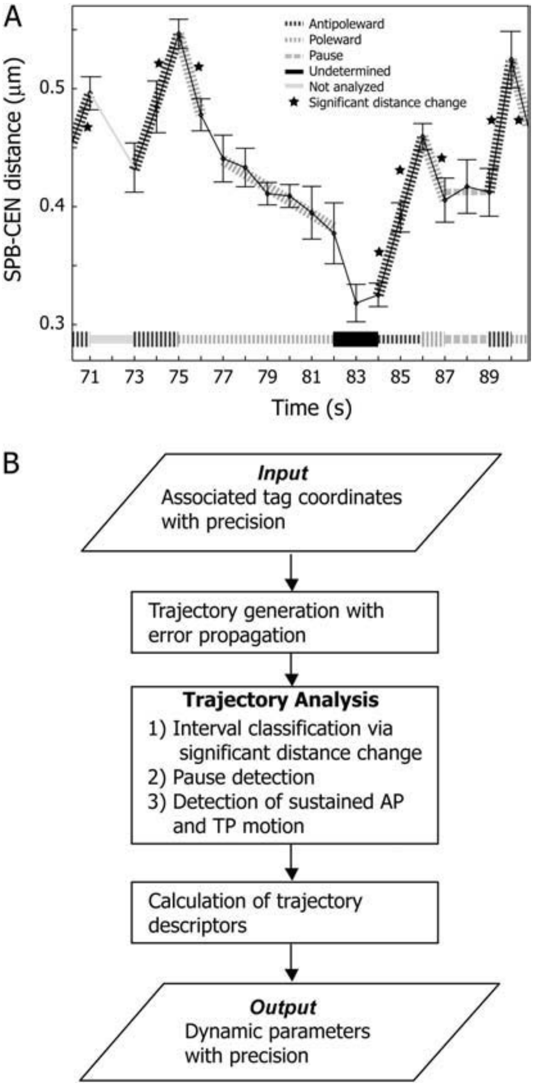

FIGURE 3 Tag distance trajectory analysis to classify microtubule dynamics. (*A*) SPB-CEN distance trajectories (*black solid line*), are partitioned into periods of antipoleward (AP, *dark gray dashed line*) and poleward (TP, *light gray dashed line*) movements and pause (*light gray dotted line*). Undetermined periods remain black. Intervals containing deleted frames (*gray solid line*) are not analyzed. Each distance value is attributed with a 66% confidence interval, derived from noise estimates in the raw image. These uncertainty estimates are exploited by the classification scheme to formulate a series of statistical tests (see Materials and Methods). Asterisks mark trajectory intervals between consecutive time points with statistically significant AP and TP movements. These intervals are then expanded to longer periods of AP and TP movement, if adjacent, initially insignificant intervals provide sufficient ensemble evidence for either of the movement classes. Bars at the bottom of the panel encode the classification of movements used for the calculation of the frequencies of directional switches. (*B*) Flowchart of the classification algorithm.

presence of measurement noise it is very difficult to unambiguously define turning points. We have therefore designed a statistical classification scheme that identifies the most probable mode of motion in every frame while accounting for the signal- and time-dependent uncertainty of the SPB-CEN distance (as derived from the raw image data by error propagation in MMF and MTM; see above). Intervals between consecutive time points in the raw trajectory (Fig. 3 *A*, *black*) are classified in three steps, as outlined in Fig. 3 *B*. Intervals spanning missing frames (Fig. 3 *A*, *gray*) are not classified. The following symbols are used in the statistical tests: $H_0$, null hypothesis; $H_A$, alternative hypothesis; $\sigma$, standard deviation; $T$, test statistic; $N(0,1)$, standard normal distribution; $t(n)$, Student's $t$-distribution with $n$ degrees of freedom; $F(n,m)$, $F$-distribution with $n$,$m$ degrees of freedom; $\alpha$, significance level ($p$-value at which null hypothesis is rejected). The significance levels have been selected to result in a conservative classification that will not assign a state of motion in an ambiguous case. i), Every interval between valid, consecutive frames is tested separately for a significant change in distance:

$$H_0 : d_i = d_{i+1}; H_A : d_i \neq d_{i+1}; \quad T = \frac{d_{i+1} - d_i}{\sqrt{\sigma^2_{d_{i+1}} + \sigma^2_{d_i}}} \sim N(0,1); \alpha = 0.05, \tag{5}$$

where $d_{i,i+1}$ denote SPB-CEN distances in two consecutive frames at the time points $t_i$ and $t_{i+1}$. In this test, the number of voxels employed in the fitting of the positions is much larger than the number of free parameters for both the MMF and the MTM algorithms. Thus, we apply the normal distribution instead of Student's $t$-distribution because of the large number of degrees of freedom. If the null hypothesis is rejected, the SPB-CEN distance change is classified as AP or TP depending on the sign of $d_{i+1} - d_i$ (Fig. 3 *A*, *asterisks*). Otherwise, the interval remains undetermined (e.g., interval 82–83 s in Fig. 3 *A*). ii), All groups of at least two consecutive, undetermined intervals are tested for the possibility that they represent a pause. We test whether a line fit with the slope as a free parameter ($S$, corresponding to a no-pause condition) represents the $n$ data points associated with a sequence of as-yet undetermined intervals ($n \geq 3$) no better than a line fit with a slope constrained to zero ($P$, pause condition). The test relies on the $\chi^2$-statistics of the residuals of the two fits:

$$H_0 : \chi^2_P = \chi^2_S; H_A : \chi^2_P > \chi^2_S; T = \frac{\chi^2_P}{\chi^2_S} \sim F(n-2, n-1); \alpha = 0.3. \tag{6}$$

Furthermore, we test if any of the $n$ points is an outlier:

$$H_0 : \varepsilon_i = 0; H_A : \varepsilon_i \neq 0; T = \frac{\varepsilon_i}{\sigma_i} \sim t(n-1); \alpha = 0.25; i = 1 \dots n, \tag{7}$$

where $\varepsilon_i$ is the residual, i.e., the difference between $d_i$ and the zero slope fit line, and $\sigma_i$ denotes the a posteriori uncertainty of the residual (29). If any of the two null hypotheses in Eqs. 6 or 7 is rejected, the pause hypothesis as a whole is rejected. The group of $n$ data points is then replaced by two overlapping groups of $n - 1$ data points each, and classification according to Eqs. 6 and 7 is repeated, until the number of data points per group reaches the minimum number of 3 (i.e., the number of intervals reaches 2). Intervals that cannot be classified as a pause remain undetermined. Consequently, a pause is at least two intervals long (e.g., 87–89 s in Fig. 3 *A*). iii), We test for sustained AP and TP motion by grouping consecutive intervals classified as either undetermined or AP, or as either undetermined or TP motion. Each group of $n$ SPB-CEN distances is fitted with a line of the form $d_i = a_0 + a_1 t_i$. This line fit is tested for a nonzero slope

$$H_0 : a_1 = 0; H_A : a_1 \neq 0; T = \frac{a_1}{\sigma_{a_1}} \sim t(n-2); \alpha = 0.05, \tag{8}$$

and for zero outliers

$$H_0 : \varepsilon_i = 0; H_A : \varepsilon_i \neq 0; T = \frac{\varepsilon_i}{\sigma_i} \sim t(n-2); \alpha = 0.25; i = 1 \dots n. \tag{9}$$

As defined in Eq. 7, $\varepsilon_i$ and $\sigma_i$ denote the residual and its a posteriori uncertainty of $d_i$ to the line fit. If the null hypothesis in Eq. 8 is rejected and the null hypothesis in Eq. 9 is accepted for all data points, the group of intervals is classified as an event of sustained AP or TP motion (Fig. 3 *A*, 73–75 and 77–82 s, respectively). If an interval that has previously been classified as TP or AP motion is merged with other intervals, its parameters are replaced by those of the new line fit. For example, in Fig. 3 *A*, the speed of the interval from 74 to 75 s is replaced by the speed calculated from the slope of the line fit spanning the intervals from 73 to 75 s. If the null hypothesis in Eq. 8 is accepted, or any of the null hypotheses in Eq. 9 is rejected, the fit is discarded, and the group of $n$ data points is replaced by two overlapping groups of $n - 1$ data points each. In these two intervals, the tests for sustained AP or TP motion are repeated until the number of data points per group reaches the minimum number of 3. Previously undetermined intervals that cannot be merged into events of sustained AP or TP motion remain undetermined.

In a manual classification of MT dynamics, one would probably assign the entire period 75–83 s to TP motion. Our statistical classification, however, rejects a linear fit to the entire period because of outliers, whose presence indicates that a significant change in TP motion occurs in this part of the trajectory. Accordingly, the scheme splits the period into two shorter events with significantly different TP speeds (75–76 and 77–82 s). The changes in distance in the intervals 76–77 and 82–83 s are not significant on their own at a confidence level $(1 - \alpha) = 0.95$ (Eq. 5). At the same time, the changes in distance in the two intervals are too different from the changes in distance in the adjacent intervals to be merged into a longer fit. Thus, motion in these intervals remains undetermined.

The classification of trajectories into subbranches allows us to extract not only the mean speeds of MT dynamics, but also provides hitherto unevaluated information on the heterogeneity of velocities during AP and TP motion. As will be shown in the Results and Discussion sections, we find that the distribution of these velocities may be indicative of changes in the regulation of MT dynamics.

As a consequence of the partitioning of trajectories into subbranches, the classification yields a sizeable amount of undetermined intervals. Because pauses have to be at least two intervals long to allow a statistical test for zero motion, the undetermined intervals can either originate from short motion pauses that are not detectable with this classification scheme, or from displacements that were small compared to the positional uncertainties. Not accounting for very small displacements potentially leads to a slight overestimation of AP and TP speeds. Because the proportion of undetermined intervals is similar for all conditions reported (Table 1), however, such an overestimation would be similar for all conditions and is therefore unlikely to affect their discrimination.

In calculating the frequencies of switching from AP to TP motion and vice versa, we are only interested in the time the MT spends in a state of either AP or TP motion (*horizontal bars* at the *bottom* of Fig. 3 *A*). Periods of same directionality can be either adjacent or separated by a pause or a single undetermined interval (33,34). For example, the undetermined interval 76–77 s is grouped into a state of general TP motion (*red horizontal bar* at the *bottom* of Fig. 3 *A*). This is not possible for the interval 82–83 s, as there is no way to statistically determine when the switch from TP (75–82 s) to AP (84–86 s) motion occurs.

## RESULTS

We analyzed the joint motion of SPB and CEN tag on the unreplicated chromosome IV during the G1 phase of the budding yeast cell cycle. In each cell we calculated the distance

**TABLE 1 Descriptors of interphase (G1) centromere movement in budding yeast**

| | WT 37°C | WT 37°C w/ benomyl | *ndc10-1* 37°C | *ndc10-1* 37°C w/ benomyl |
|---|---|---|---|---|
| AP-to-TP frequency (1/s) | 0.70 ± 0.02 (650) | 0.62 ± 0.02 (653) | 0.65 ± 0.02 (468) | 0.64 ± 0.02 (401) |
| TP-to-AP frequency (1/s) | 0.75 ± 0.02 (683) | 0.75 ± 0.02 (751) | 0.74 ± 0.02 (528) | 0.73 ± 0.02 (446) |
| Antipoleward speed ($\mu$m/min) | 6.46 ± 0.15 (715) | 4.26 ± 0.11 (793) | 9.28 ± 0.20 (613) | 8.90 ± 0.23 (530) |
| Poleward speed ($\mu$m/min) | 6.17 ± 0.16 (689) | 4.43 ± 0.11 (768) | 9.16 ± 0.22 (590) | 8.74 ± 0.23 (518) |
| Mean distance ($\mu$m) | 0.63 ± 0.01 (4820) | 0.50 ± 0.00 (3914) | 1.23 ± 0.01 (2145) | 1.22 ± 0.01 (1804) |
| SD of distance ($\mu$m) | 0.09 ± 0.00 (4820) | 0.11 ± 0.01 (3914) | 0.22 ± 0.01 (2145) | 0.20 ± 0.12 (1804) |
| Minimum distance ($\mu$m) | 0.220 ± 0.024 | 0.224 ± 0.011 | 0.245 ± 0.036 | 0.305 ± 0.043 |
| Maximum distance ($\mu$m) | 1.729 ± 0.021 | 1.379 ± 0.011 | 2.505 ± 0.016 | 2.125 ± 0.011 |
| Antipoleward time (s) | 923 (=21.1%) | 1047 (=27.6%) | 721 (=34.9%) | 624 (=37.1%) |
| Poleward time (s) | 914 (=20.9%) | 996 (=26.3%) | 714 (=34.5%) | 609 (=36.3%) |
| Pause time (s) | 534 (=12.2%) | 253 (=6.7%) | 77 (=3.7%) | 16 (=1.0%) |
| Undetermined time (s) | 1995 (=45.7%) | 1498 (=39.5%) | 556 (=26.9%) | 431 (=25.7%) |

| | WT 34°C | WT 34°C w/ benomyl | WT 25°C | *tub2-150* 34°C w/ benomyl | *tub2-150* 34°C |
|---|---|---|---|---|---|
| AP-to-TP frequency (1/s) | 0.63 ± 0.02 (382) | 0.61 ± 0.02 (438) | 0.65 ± 0.02 (382) | 0.66 ± 0.02 (577) | 0.62 ± 0.02 (526) |
| TP-to-AP frequency (1/s) | 0.80 ± 0.02 (433) | 0.72 ± 0.02 (498) | 0.74 ± 0.02 (424) | 0.76 ± 0.02 (667) | 0.77 ± 0.02 (569) |
| Antipoleward speed ($\mu$m/min) | 4.74 ± 0.13 (465) | 4.22 ± 0.12 (519) | 3.92 ± 0.12 (458) | 5.01 ± 0.13 (695) | 5.17 ± 0.13 (648) |
| Poleward speed ($\mu$m/min) | 4.86 ± 0.14 (424) | 4.31 ± 0.12 (493) | 3.99 ± 0.12 (433) | 4.92 ± 0.11 (705) | 5.61 ± 0.14 (590) |
| Mean distance ($\mu$m) | 0.53 ± 0.00 (2199) | 0.47 ± 0.00 (3204) | 0.48 ± 0.00 (2212) | 0.59 ± 0.00 (3115) | 0.54 ± 0.00 (3050) |
| SD of distance ($\mu$m) | 0.10 ± 0.01 (2199) | 0.09 ± 0.01 (3204) | 0.08 ± 0.01 (2212) | 0.10 ± 0.00 (3115) | 0.11 ± 0.01 (3050) |
| Minimum distance ($\mu$m) | 0.244 ± 0.010 | 0.206 ± 0.017 | 0.196 ± 0.005 | 0.197 ± 0.006 | 0.215 ± 0.15 |
| Maximum distance ($\mu$m) | 1.138 ± 0.021 | 1.146 ± 0.041 | 0.949 ± 0.042 | 1.427 ± 0.034 | 1.272 ± 0.022 |
| Antipoleward time (s) | 603 (=28.8%) | 721 (=23.8%) | 589 (=27.0%) | 876 (=28.7%) | 848 (=29.5%) |
| Poleward time (s) | 539 (=25.7%) | 691 (=22.9%) | 570 (=26.2%) | 879 (=28.8%) | 741 (=25.8%) |
| Pause time (s) | 122 (=5.8%) | 305 (=10.1%) | 199 (=9.1%) | 228 (=7.5%) | 219 (=7.6%) |
| Undetermined time (s) | 832 (=39.7%) | 1307 (=43.2%) | 820 (=37.6%) | 1068 (=35.0%) | 1069 (=37.2%) |

between SPB and CEN tag. This distance reflects the length of the MT in the case of attached chromosomes. As described in Methods, the SPB-CEN distance is invariant to drift of the microscope stage and to rotation of the yeast nucleus (35), both of which can be prominent over the course of a single movie (Fig. 4 *A*). In our analysis, the uncertainty associated with each distance measurement was derived from the SNR of the raw movie and propagated by the tracking algorithms (Fig. 2). The distance uncertainties depend on three factors: i), tracking method. Tags resolved by only MTM (Fig. 4 *B*, *light gray circles*) systematically had larger uncertainties than tags localized by MMF (Fig. 4 *B*, *dark gray stars*). This originates from the fact that the uncertainties of tags resolved by MTM are a sum of two uncertainties: the uncertainties in tag positions in the source frame as calculated by the MMF algorithm, and the uncertainty of displacement of these tags between source and target frame as calculated by the MTM algorithm. ii), SNR. Both MTM and MMF uncertainties increased over the duration of a movie because of photobleaching, which reduced the SNR of tags in late frames of a movie (Fig. 1 *B*). iii), Orientation of the SPB-CEN axis. As indicated by Fig. 4 *C*, the geometry of the tag configuration has the strongest influence on the distance uncertainty. Because of the oblong shape of the 3D PSF, the uncertainty in the axial component of the SPB-CEN distance vector is approximately three times larger than the uncertainty in the lateral components. Thus, distance uncertainties increase with the off-plane angle of the SPB-CEN axis (Fig. 4 *C*). Distance uncertainties at high SNR ($SNR > 8$) were ~10 nm for in-plane axes and up to 30 nm for vertical SPB-CEN axes. Uncertainties at low SNR ($SNR < 4$) were twice as large.

## Minimum observed SPB-CEN tag distance of 200 nm is above the shortest resolvable distance

Many of the resolved tag pairs in the collected SPB-CEN distance trajectories were separated by less than the inverse of the OTF cutoff frequency $L$ (Fig. 5 *A*), which is often used to define the resolution limit of the microscope (36). Using prior knowledge, methods like MMF and MTM can resolve objects that are separated by distances below $L$. This ability is sometimes referred to as ''superresolution'' (27,28,37,38). Like the uncertainty, $L$ depends on the orientation of the SPB-CEN axis. To calculate $L$ as a function of the axis off-plane angle $\theta$, we approximated the PSF by an ellipsoid, thus

$$L(\theta) = \left(\left(\frac{\cos\theta}{L_{xy}}\right)^2 + \left(\frac{\sin\theta}{L_z}\right)^2\right)^{-\frac{1}{2}},$$

where $L_{xy}$ and $L_z$ denote the inverted frequency cutoffs in lateral and axial direction. In our microscopy setup, $L_{xy}$ and $L_z$ equal 229 and 814 nm, respectively.

Using simulated data, we have previously shown that MMF can resolve tags separated by distances as small as 50 and 66% of $L(\theta)$ in images with SNR 15 and 8, respectively (15). We have also shown that, by combining MMF and MTM, the separation performance improves to 30% (SNR

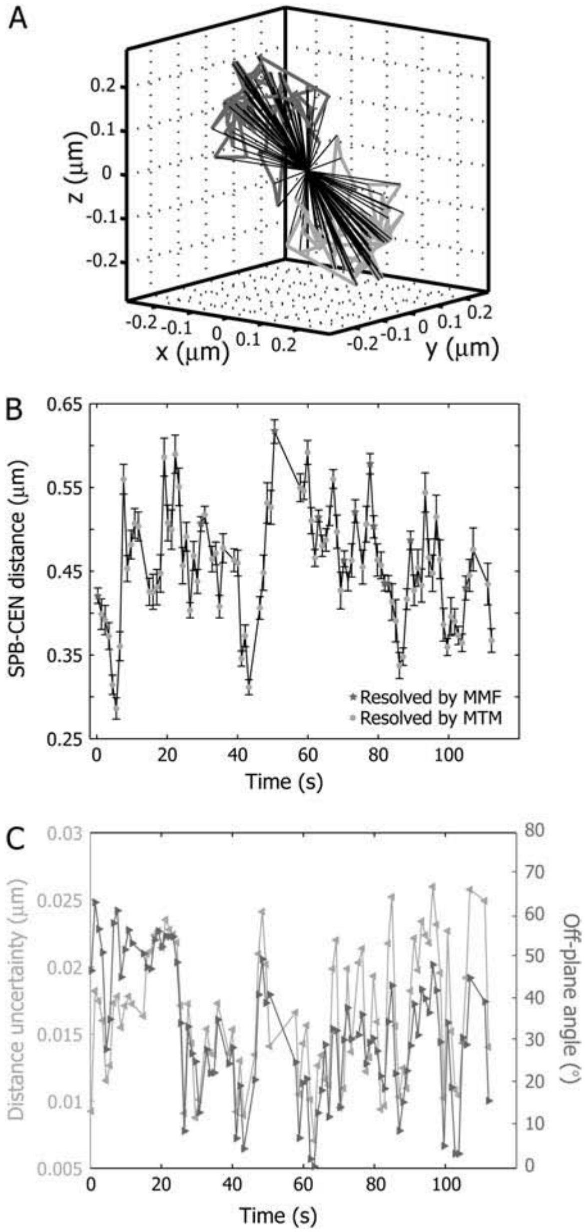

FIGURE 4 Influence of the 3D positions of spindle pole body and centromere on uncertainties in the distance between them. (*A*) Motion of SPB (*dark gray*) and CEN (*light gray*) tags in a WT cell in G1. The black lines connect the positions of the two tags at each time point, where the midpoint between each pair was taken as the origin for their coordinates at each time point. Animated SPB and CEN tag trajectories for the two movies in Fig. 1, *A-I–A-II*, are shown in supplementary movies S3 and S4. (*B*) SPB-CEN distance trajectory with distance uncertainties propagated by the tracking algorithm. Uncertainties are generally larger for distances resolved by MTM (*light gray dots*) than for distances resolved by MMF (*dark gray stars*), and they increase with increasing off-plane angle as well as toward the end of the movie as the SNR decreases. (*C*) Influence of nuclear rotation on distance uncertainty. Uncertainties (*light gray*) and corresponding off-plane angles of the SPB-CEN axis (*dark gray*) are shown to indicate how increasing off-plane angles amplify the distance uncertainty because of the narrower axial bandpass of the microscope optics.

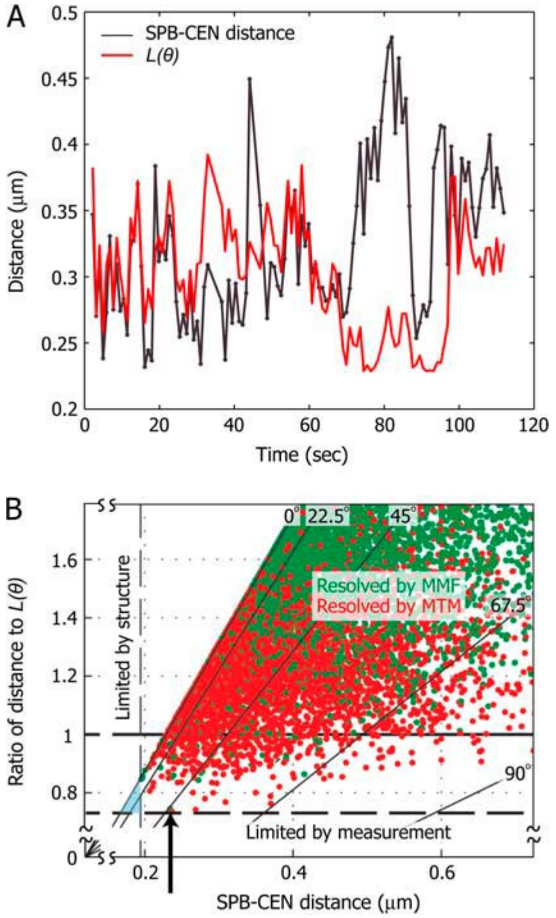

FIGURE 5 Resolution in tracking SPB-CEN distances. (*A*) SPB and CEN tags are resolved by the described image analysis even if the tag-to-tag distance (*black*) is less than the inverse of the OTF frequency cutoff (*red*; e.g., between time points 30 and 40 s the distance is up to 25% below this resolution limit). (*B*) Scatter plot of SPB-CEN distance and the ratio between SPB-CEN distance and inverse of the OTF frequency cutoff at the corresponding SPB-CEN axis orientation. The distribution is sampled by ~20,000 distance measurements. Data points with a ratio below 1 rely on the ability of MMF and MTM tag tracking to resolve spots separated by less than the inverse of the OTF frequency cutoff. Green, distances resolved by MMF; red, distances resolved by MTM. Distances could be resolved at a ratio of 0.75 (*horizontal dashed line*). See supplementary movie S5 for a visual demonstration of the resolution performance of MMF and MTM tracking. At 0° off-plane orientation of the SPB-CEN axis a ratio 0.75 corresponds to a minimum resolvable distance of 170 nm. However, our data contained no distance smaller than ~200 nm (*vertical dashed line*). The absence of data points in the blue shaded region suggests a structural limit for the experimentally found minimum SPB-CEN tag distance.

15) and 50% (SNR 8) of $L(\theta)$ (16). However, the SNR of most of the movies analyzed in this study was lower than the values used in these simulations (~4). Indeed, the statistical tests of the MMF reported a breakdown beginning at 130% of $L(\theta)$ indicating that distance resolution beyond the inverse of the OTF cutoff required the combination of MMF and MTM. Fig. 5 *B* shows all SPB-CEN distances analyzed in this article, separating the data points into those resolved by MMF (*green dots*) and those resolved by combination of

MMF and MTM (*red dots*). The vertical axis of the graph encodes the ratio between the measured distances and $L(\theta)$. The lowest ratio found in our data was 0.75 of the inverse of the OTF cutoff (*arrow* in Fig. 5 *B*). However, this measurement was captured in a frame where the SPB-CEN axis had an angle of ~45° relative to the horizontal plane, resulting in an absolute resolved distance of only ~240 nm. Assuming that the practical resolution performance of our tracking algorithm at low SNR is limited to 0.75 $L(\theta)$, we would thus expect to resolve distances down to 170 nm if the SPB-CEN axis was oriented horizontally (Fig. 5 *B*, *horizontal dashed line*). Yet, with the exception of two data points at 196 ± 5 and 197 ± 5 nm, none of the >20,000 distance measurements were below 200 nm (Fig. 5 *B*, *blue shaded triangle*). This suggests that the CEN does not approach the SPB closer than 200 nm because of a biological reason, and not due to limited performance of MMF and MTM in optically separating the CEN and SPB tags.

## Centromere motion is confined and kinetochore dependent

To test the hypothesis that chromosomes are indeed bound to MTs in G1 we compared CEN tag movements in WT and *ndc10-1* mutant cells. *Ndc10-1* mutants cannot assemble a functional kinetochore and prevent k-MTs from attaching to the chromosome (22,23). We expected that the motion of CEN tags would be much more constrained in WT than in *ndc10-1* cells.

For both strains we calculated the mean squared SPB-CEN distance change, $MSQD(\tau)$, as a function of time lag $\tau$ (see Materials and Methods)

$$MSQD(\tau) = \langle (d(t+\tau) - d(t))^2 \rangle_t,$$

where $d(t)$ denotes the magnitude of the SPB-CEN distance vector at time $t$. Both *ndc10-1* and WT cells exhibited mean squared displacements characteristic of constrained random motion (Fig. 6) (35). For long time lags ($MSQD(\tau \rightarrow \infty)$) the curves reached a plateau, which can be related to the size of the confinement region (31). In accord with our expectation, the plateau of *ndc10-1* was 4 times larger than that of WT. Assuming a random walk of the CEN tag within a spherical region with the SPB fixed at a point on its surface, we estimated a radius of the confinement sphere of ~0.27 $\mu$m for WT at 37°C and ~0.52 $\mu$m for *ndc10-1* (cf. Eq. 3). The radius of the yeast nucleus in G1 is between 0.5 and 0.75 $\mu$m, indicating that the centromere in *ndc10-1* cells could sample the entire volume of the nucleus. Also, *MSQD* curves of WT CEN tag movements reached a plateau at significantly shorter time lags than those of *ndc10-1*. This provides additional support for a much tighter coupling of CEN and SPB tag movement in WT as compared to *ndc10-1* cells. The *MSQD* curves reach a plateau at time lags above 100 s. Stable calculation of *MSQD* at these time lags requires trajectories lasting at least 400 s (30). However, the GFP tags bleached almost completely in 100-s movies with 1-s sampling (Fig. 1), making accurate tracking impossible for 400-s movies with 1-s sampling. We therefore relied on movies with 5-s sampling.

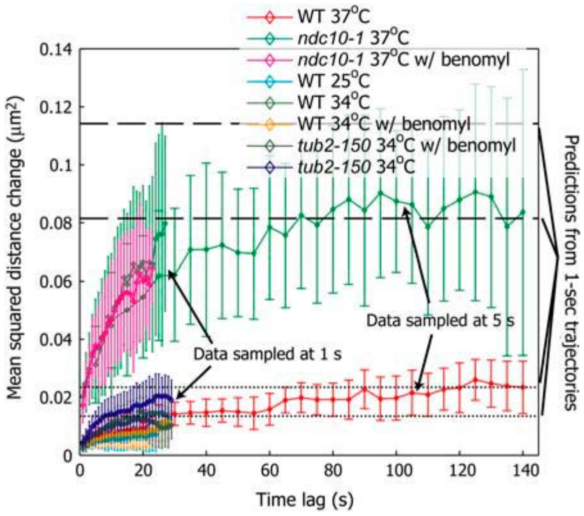

FIGURE 6 Mean squared SPB-CEN distance change versus time lag. CEN-tag movements in *ndc10-1* strains are substantially less constrained than in WT or *tub2-150*. The latter strains are indistinguishable by MSQD statistics. Data sampled at a frame rate of 1/s follow the same trend as data sampled at a frame rate 1/(5 s) and would reach the same plateau of constrained diffusional motion. Ranges of the MSQD plateau for constrained diffusion extrapolated from 1-s trajectories are indicated for *ndc10-1* (*dashed lines*) and WT and *tub2-150* (*dotted lines*).

Alternatively, as outlined in Materials and Methods, it was possible to extrapolate the size of the confinement region from the mean standard deviation $\sigma$ of the SPB-CEN distance (Eq. 4), using data from 100-s movies with 1-s sampling, in which the plateau had not been reached. Values of $\sigma$ (Table 1) correspond to confinement radii of $R_C = 0.55 \pm 0.03$ $\mu$m for *ndc10-1* and $R_C = 0.23 \pm 0.01$ $\mu$m for WT at 37°C, in good agreement with the 5-s data. Plateau values of *MSQD* estimated from 1-s trajectories are shown in Fig. 6 as dashed lines for *ndc10-1* and as dotted lines for WT. We concluded that, by combination of Eqs. 3 and 4, the plateau $MSQD(\tau \rightarrow \infty)$ is predictable even for trajectories that are too short to exhibit a plateau in the *MSQD* graphs. These data support our hypothesis that CEN tags are more constrained in WT than in *ndc10-1* cells and thus, that kinetochores are required for confining centromeres.

## Centromere motion is dependent on k-MT dynamics

WT SPB-CEN distance trajectories also displayed the characteristics of diffusional motion (Fig. 6). However, we hypothesized that the constrained random walk of CEN tags in WT cells was the consequence of kinetochore attachment to k-MTs that were undergoing dynamic instability. To test this hypothesis, we analyzed WT cells at 37, 34, and 25°C, and compared the WT phenotype at 34°C to *tub2-150*, a yeast $\beta$-tubulin mutant requiring the MT destabilizing drug benomyl for viability, in the presence and absence of benomyl. We expected that, if CEN tag movement was dependent on k-MT attachment, these perturbations that are known to affect MT dynamics, would lead to significant responses in the dynamic phenotypes of the cells. As a control, we also analyzed the dynamic phenotype of *ndc10-1* in the presence and absence of benomyl. We expected benomyl to have no effect on CEN-tag trajectories in a mutant where chromosomes were detached.

Simple *MSQD* statistics did not provide the sensitivity to distinguish between these more subtle phenotypes. We therefore switched to descriptors that had been used extensively to characterize MT dynamics (32,33). We divided a trajectory into periods of AP motion, TP motion, and pauses (see Materials and Methods). Importantly, our statistical classification scheme included an analysis of speed variation throughout periods of AP and TP motion, allowing us to compare MT dynamics under various experimental conditions based not only on mean speeds, but also on speed distributions. We used this classification to calculate descriptors of chromosome dynamics, as listed in Table 1, along with more static measures, such as average SPB-CEN distance. Fig. 7 summarizes the differences in AP speeds and TP speeds for the different experimental conditions in discrimination matrices. The differences between speeds in each condition were analyzed using two statistical tests: below the diagonals, the mean speeds were compared with a Student's *t*-test for two independent samples with unequal variance (Behrens-Fisher problem, (39)); above the diagonal, speed distributions were compared using a Kolmogorov-Smirnov test (39), which tests the maximal deviation between cumulative distributions for its significance. To ensure that the Kolmogorov-Smirnov test detected significant differences only if the distributions differed in shape, but not in the mean, the two distributions were aligned at their mean before testing (supplemental Fig. S6). Field gray levels encode the significance level of the difference in speed between the experimental condition in the corresponding row and column. The numerical value is the *p*-value for classifying identical averages or distributions as different. Statistical analyses of other descriptors, such as the average SPB-CEN distance, or the AP-to-TP or the TP-to-AP frequencies were of limited use in distinguishing between the phenotypes presented here. Although the switching frequencies of k-MTs were very different from those of cytoplasmic MTs reported in the literature (see Discussion), they did not vary significantly between the conditions examined in this article. Conversely, the average SPB-CEN distances were significantly different in all instances and hence were not useful for differentiating phenotypes.

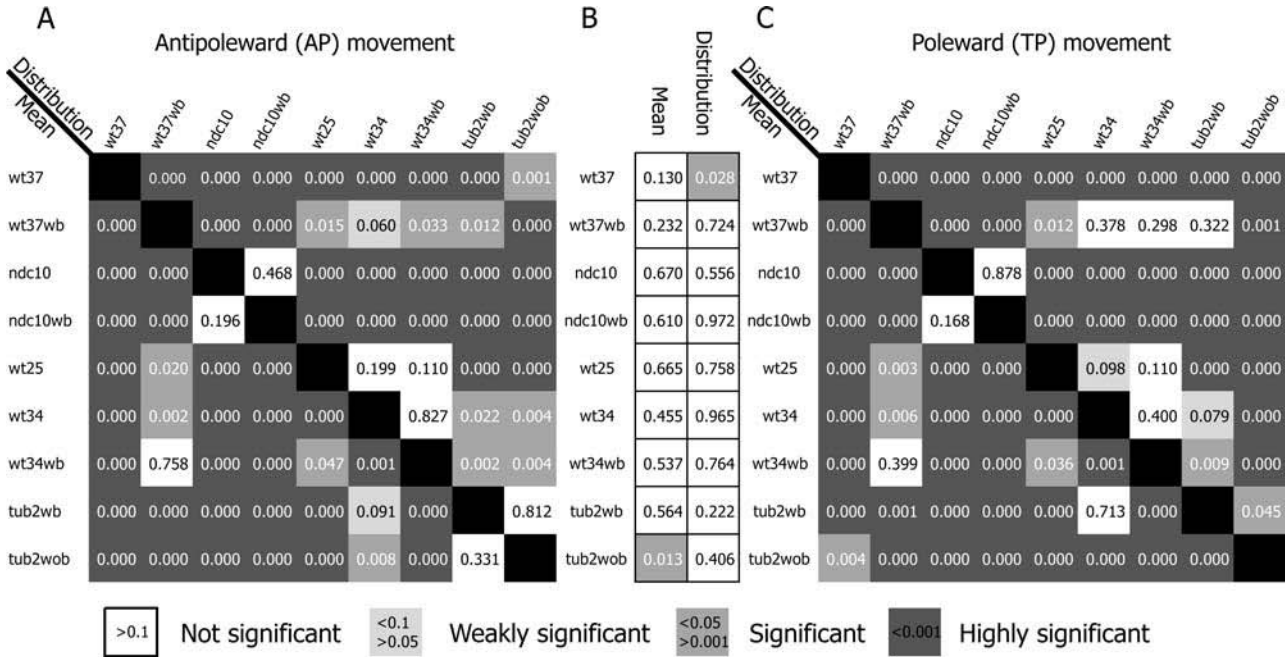

A

Antipoleward (AP) movement

| Distribution / Mean | wt37 | wt37wb | ndc10 | ndc10wb | wt25 | wt34 | wt34wb | tub2wb | tub2wob |
|---|---|---|---|---|---|---|---|---|---|
| wt37 | | 0.000 | 0.000 | 0.000 | 0.000 | 0.000 | 0.000 | 0.000 | 0.001 |
| wt37wb | 0.000 | | 0.000 | 0.000 | 0.015 | 0.060 | 0.033 | 0.012 | 0.000 |
| ndc10 | 0.000 | 0.000 | | 0.468 | 0.000 | 0.000 | 0.000 | 0.000 | 0.000 |
| ndc10wb | 0.000 | 0.000 | 0.196 | | 0.000 | 0.000 | 0.000 | 0.000 | 0.000 |
| wt25 | 0.000 | 0.020 | 0.000 | 0.000 | | 0.199 | 0.110 | 0.000 | 0.000 |
| wt34 | 0.000 | 0.002 | 0.000 | 0.000 | 0.000 | | 0.827 | 0.022 | 0.004 |
| wt34wb | 0.000 | 0.758 | 0.000 | 0.000 | 0.047 | 0.001 | | 0.002 | 0.004 |
| tub2wb | 0.000 | 0.000 | 0.000 | 0.000 | 0.000 | 0.091 | 0.000 | | 0.812 |
| tub2wob | 0.000 | 0.000 | 0.000 | 0.000 | 0.000 | 0.008 | 0.000 | 0.331 | |

B

| | Mean | Distribution |
|---|---|---|
| wt37 | 0.130 | 0.028 |
| wt37wb | 0.232 | 0.724 |
| ndc10 | 0.670 | 0.556 |
| ndc10wb | 0.610 | 0.972 |
| wt25 | 0.665 | 0.758 |
| wt34 | 0.455 | 0.965 |
| wt34wb | 0.537 | 0.764 |
| tub2wb | 0.564 | 0.222 |
| tub2wob | 0.013 | 0.406 |

C

Poleward (TP) movement

| Distribution / Mean | wt37 | wt37wb | ndc10 | ndc10wb | wt25 | wt34 | wt34wb | tub2wb | tub2wob |
|---|---|---|---|---|---|---|---|---|---|
| wt37 | | 0.000 | 0.000 | 0.000 | 0.000 | 0.000 | 0.000 | 0.000 | 0.000 |
| wt37wb | 0.000 | | 0.000 | 0.000 | 0.012 | 0.378 | 0.298 | 0.322 | 0.001 |
| ndc10 | 0.000 | 0.000 | | 0.878 | 0.000 | 0.000 | 0.000 | 0.000 | 0.000 |
| ndc10wb | 0.000 | 0.000 | 0.168 | | 0.000 | 0.000 | 0.000 | 0.000 | 0.000 |
| wt25 | 0.000 | 0.003 | 0.000 | 0.000 | | 0.098 | 0.110 | 0.000 | 0.000 |
| wt34 | 0.000 | 0.006 | 0.000 | 0.000 | 0.000 | | 0.400 | 0.079 | 0.000 |
| wt34wb | 0.000 | 0.399 | 0.000 | 0.000 | 0.036 | 0.001 | | 0.009 | 0.000 |
| tub2wb | 0.000 | 0.001 | 0.000 | 0.000 | 0.000 | 0.713 | 0.000 | | 0.045 |
| tub2wob | 0.004 | 0.000 | 0.000 | 0.000 | 0.000 | 0.000 | 0.000 | 0.000 | |

| >0.1 | Not significant |
|---|---|
| <0.1 >0.05 | Weakly significant |
| <0.05 >0.001 | Significant |
| <0.001 | Highly significant |

FIGURE 7 Discrimination of phenotypes based on MT (SPB-CEN distance) dynamics. (*A*) Discrimination based in antipoleward (*AP*) speeds. Values below the diagonal indicate the *p*-values for the null hypothesis that the mean speed between two experimental conditions is equal. Values above the diagonal indicate *p*-values for the null hypothesis that the aligned speed distributions are equal. Gray levels encode the significance level (1 − *p*-value) for two mean speeds or distributions being different. (*B*) Comparison of AP and TP speeds within one experimental condition. Left column, difference between AP and TP mean speeds; right column, difference between AP and TP speed distributions. (*C*) Discrimination based on poleward (*TP*) speeds. Abbreviations: w(o)b, with(out) benomyl; ndc10, *ndc10-1*; tub2, *tub2-150*. wtXX, WT at *XX*°C.

Below, we summarize the data in Table 1. We explain how movements of the CEN tag relative to the SPB tag support the hypothesis that chromosome dynamics are MT dependent. This leads us to conclude that, in contrast to metazoan cells, interphase chromosomes are attached to dynamic MTs in budding yeast.

1. *ndc10-1* versus WT. Speeds of AP and TP motion of detached CEN tags in *ndc10-1* at 37°C were significantly higher than those in WT at 37°C. Exposure to 40 $\mu$g/ml of benomyl significantly changed both the mean and the distribution of AP and TP speeds in WT cells, but not in *ndc10-1* cells. These data indicate that a functional kinetochore is required for the MT destabilizing drug benomyl to have an effect on centromere motion, suggesting that yeast chromosomes are attached to k-MTs in G1.
2. WT at 25, 34, and 37°C. Increasing the temperature in WT cells from 25 to 37°C increased AP and TP speed in a nonlinear way: Speeds increased by ~0.8 $\mu$m/min from 25 to 34°C, and by ~1.4 $\mu$m/min from 34 to 37°C. The distributions of both AP and TP speeds at 37°C differed from the distributions at 34 and 25°C in a highly significant way, whereas the differences between the distributions of TP and AP speeds between WT at 34 and 25°C were either weakly or not significant (see also supplemental Fig. S6). This nonlinear change in speeds indicates that the motion of the CEN tag is not simply diffusive, but depends on the regulation of MT dynamics with temperature.
3. WT at 34 and 37°C with benomyl. Exposure of WT cells to 40 $\mu$g/ml of benomyl at 34°C did not depolymerize k-MTs completely, although it decreased the average SPB-CEN distance from 530 to 470 nm, which was close to the 480 nm found for WT at 25°C. Dynamic descriptors of WT at 34°C with benomyl also appeared closer to those of WT at 25°C than to those of WT at 34°C without benomyl. The differences in both AP and TP speeds between WT at 34°C with benomyl and WT at 25°C were weak, whereas they were highly significant between WT at 34°C with and without benomyl. Exposure of WT cells to benomyl at 37°C had a qualitatively similar, but quantitatively much stronger effect on the dynamics. Benomyl exposure not only decreased AP and TP speeds from $>6$ $\mu$m/min to $<4.5$ $\mu$m/min, but also changed both AP and TP speed distributions, thereby almost eliminating the difference between the unperturbed cells at 34 and 37°C. WT at 34°C with benomyl is almost indistinguishable from WT at 37°C with benomyl, except for the significant difference in the distributions of AP speeds. These data suggest that benomyl exposure attenuates MT dynamics similarly to a temperature decrease.
4. *tub2-150* with and without benomyl. As was to be expected, *tub2-150* at 34°C under permissive conditions, i.e., in the presence of 40 $\mu$g/ml of benomyl, was very close to WT at 34°C. The average TP speeds for both strains could not be distinguished, and the difference in speed distributions was only weakly significant. AP speeds exhibited a somewhat stronger difference, but it was still weak compared to differences to other conditions. The average SPB-CEN distance was ~60 nm longer in the mutant than in WT.

   Growing cells in the absence of benomyl, i.e., changing to nonpermissive conditions, did not affect *tub2-150* in the same way as WT cells. To our surprise, there was a highly significant increase in the TP speed as compared to *tub2-150* with benomyl, whereas AP speed remained statistically indistinguishable. This resulted in *tub2-150* without benomyl being the only condition where AP and TP speeds were significantly different. Unlike WT, the average SPB-CEN distance was lower without benomyl.

Together, these results underline the attachment of chromosomes in G1 and the dependence of CEN tag motion on k-MT dynamics. We thus promote the model of kinetochore-dependent attachment of chromosomes in G1 and propose our method of tracking and classifying SPB-CEN tag trajectories as a sensitive assay for probing experimental conditions that affect the properties of nuclear MT dynamics.

## DISCUSSION

Many biological mechanisms, such as cell cycle progression and secretion, have been successfully dissected based on obvious phenotypes that were derived from relatively simple readouts, e.g., morphologic or colorimetric measurements. However, for the study of space- and time-dependent dynamical systems like the actin cytoskeleton or the spindle apparatus, the definition of informative, yet easy readouts is more difficult. Because these systems include redundant components, even strong perturbations may lead to only a subtle phenotype. For example, the kinetochore and tubulin mutants examined in this article both have ultimately lethal phenotypes but their effects on spindle dynamics appeared to be relatively minor. To understand the evidently critical roles of such genes in the context of a complex process, multidimensional readouts of cell states that are sensitive enough to differentiate between mild variations of phenotypes must be developed.

In our study of the function of kinetochore proteins in the spindle apparatus, we establish single chromosome dynamics as a sensitive readout for alterations in the regulation of k-MT dynamics. We demonstrate that the tracking of the motion of a single chromosome relative to the SPB in budding yeast and the subsequent thorough statistical analysis of the distance trajectories allows us to distinguish between molecular and environmental conditions that induce minute changes in the k-MT-dependent dynamics of chromosomes. Budding yeast is particularly suitable for this study because it has only one MT per sister chromatid, which means that the kinetochore regulates one MT only. Furthermore, budding yeast k-MTs do not treadmill (10), and so chromosome motion is the direct result of the growth and shrinkage of the plus-end of one MT only.

However, the advantages of yeast as an organism in which to study kinetochores come at the price of several technological challenges. The yeast spindle is only $\sim$1.5 $\mu$m long, which is very small compared to $\sim$25 $\mu$m for *Xenopus* spindles, and MT dynamics are fast. Fluorescence recovery after photobleaching experiments on yeast half-spindles (10) have suggested that MT treadmilling does not occur in yeast, but this very difficult assay cannot distinguish between the dynamics of kinetochore and interpolar MTs. Labeling the centromere-specific histone Cse4p (7) can circumvent this problem, but the superposition of tag signals from the 16 chromosomes reduces the readout from individual k-MT dynamics to average fluorescence distributions. Relating this readout to the underlying k-MT dynamics is a complicated process (40), the sensitivity and uniqueness of which has not yet been demonstrated.

To measure and analyze the dynamics of individual k-MTs, we have tagged the SPB and a CEN-proximal region on chromosome IV, and have developed automated image analysis software that allows us to process efficiently a large number of 3D movies. The software resolves and localizes the CEN and SPB tags in 3D despite the frequent overlap of their signals and their low SNR. We have also developed software to analyze SPB-CEN distance trajectories within the framework of statistical hypothesis testing. This yields descriptors that characterize the k-MT dynamics and allows us to distinguish between WT and mutant phenotypes.

Below, we discuss the technological requirements for sensitive analysis of MT dynamics in yeast and demonstrate the success of our assay in meeting the requirement. We then turn to the interpretation of our data in terms of k-MT dynamics and their regulation.

## CEN tag faithfully reports MT-tip dynamics

We tagged a centromere proximal region on chromosome IV with GFP as shown in Fig. 8 *A*. In our analysis, we assume that the tag is a reporter of k-MT tip dynamics, an assumption that has been controversial (7,40). Chromosome tags comprise arrays of TetO binding sites with a finite length (11 kb) and are located off the centromere by a small distance (1.1 kb). To analyze the extent to which the offset of the tag from the centromere might disturb trajectories and affect the classification, we modeled the thermal motion of the tag as a rotational diffusion (with fixed offset) about the centromere superimposed on a kinetic Monte Carlo simulation of MT dynamics, as described in the Appendix. To calculate the length of the offset, we had to make assumptions about chromosome compaction relative to B-form DNA, which has a length of 0.34 nm per basepair. As a worst case scenario we set the lower limit of compaction as the one that would just result in a subresolution GFP tag, i.e., a tag that was just shorter than 230 nm. This choice was motivated by the fact that in no single frame of our many experiments we observed a CEN tag exceeding the dimensions of the PSF. The resulting 15-fold compaction led to an offset of 160 nm. By different considerations, the compaction ratios of budding yeast G1 chromosomes have been estimated as 30-fold (41, 42), 40–50-fold (43), and 80-fold (44). Thus, our simulations also accounted for compactions that correspond with the two extreme values reported in the literature, i.e., 30- and 80-fold, which resulted in offsets of 90 and 50 nm, respectively.

Fig. 8 *B* shows the effect of tag rotation on observed AP speeds. The seven trajectories whose speeds are shown have identical parameters of MT dynamics, except for the rate of unit addition during growth ($k_{\mathrm{on}}^{\mathrm{g}}$), which increases by 5% per trajectory index. As expected, when MT-tip trajectories were perturbed by tag rotation, speeds deviated from their original values. These deviations generally increased with increasing offset and diffusion constant.

At 1-s sampling our assay inherently suffers from undersampled trajectories (see below). Therefore, it is not possible to link measured speed values to molecular processes in an absolute sense. However, our goal in this work is not the reconstruction of k-MT growth and shrinkage at the molecular scale, but employing statistics of growth and shrinkage speeds to distinguish between different phenotypes and to identify molecular mechanisms that alter the k-MT dynamics. Therefore, we had to critically examine the influence of the tag offset on the sensitivity of speed values in reporting such molecular variations.

Fig. 8 *C* demonstrates the ability of the calculated AP speeds to distinguish between trajectories arising from different rates of unit addition during growth. Mean speeds calculated from MT-tip trajectories were able to distinguish between five out of the six pairs of trajectories that differed by 5% in $k_{\mathrm{on}}^{\mathrm{g}}$. Mean speeds derived from trajectories with tag offsets performed comparably well at low diffusion constants. In almost all cases but those with the largest offset and highest diffusion constants, speeds could distinguish between all trajectories where $k_{\mathrm{on}}^{\mathrm{g}}$ differed by 10%. Note that slight changes in $k_{\mathrm{on}}^{\mathrm{g}}$, as well as low diffusion constants, did not change the distribution of speeds, whereas higher diffusion constants did. This means that at higher diffusion constants the type of motion is fundamentally different, i.e., it changes from mainly MT-driven motion to mainly diffusive motion.

We did the same analysis for TP speeds, and AP-to-TP and TP-to-AP frequencies. TP speeds were found to behave similarly to AP speeds. AP-to-TP and TP-to-AP frequencies, on the other hand, were not sensitive to changes in $k_{\mathrm{on}}^{\mathrm{g}}$, even without any tag offset. We repeated the above analysis for several other cases (for example, changing the rate of unit loss during shrinkage), and observed similar behavior for all four characteristics.

Our analysis shows that the superposition of tag rotation onto k-MT dynamics does not distort the trajectories

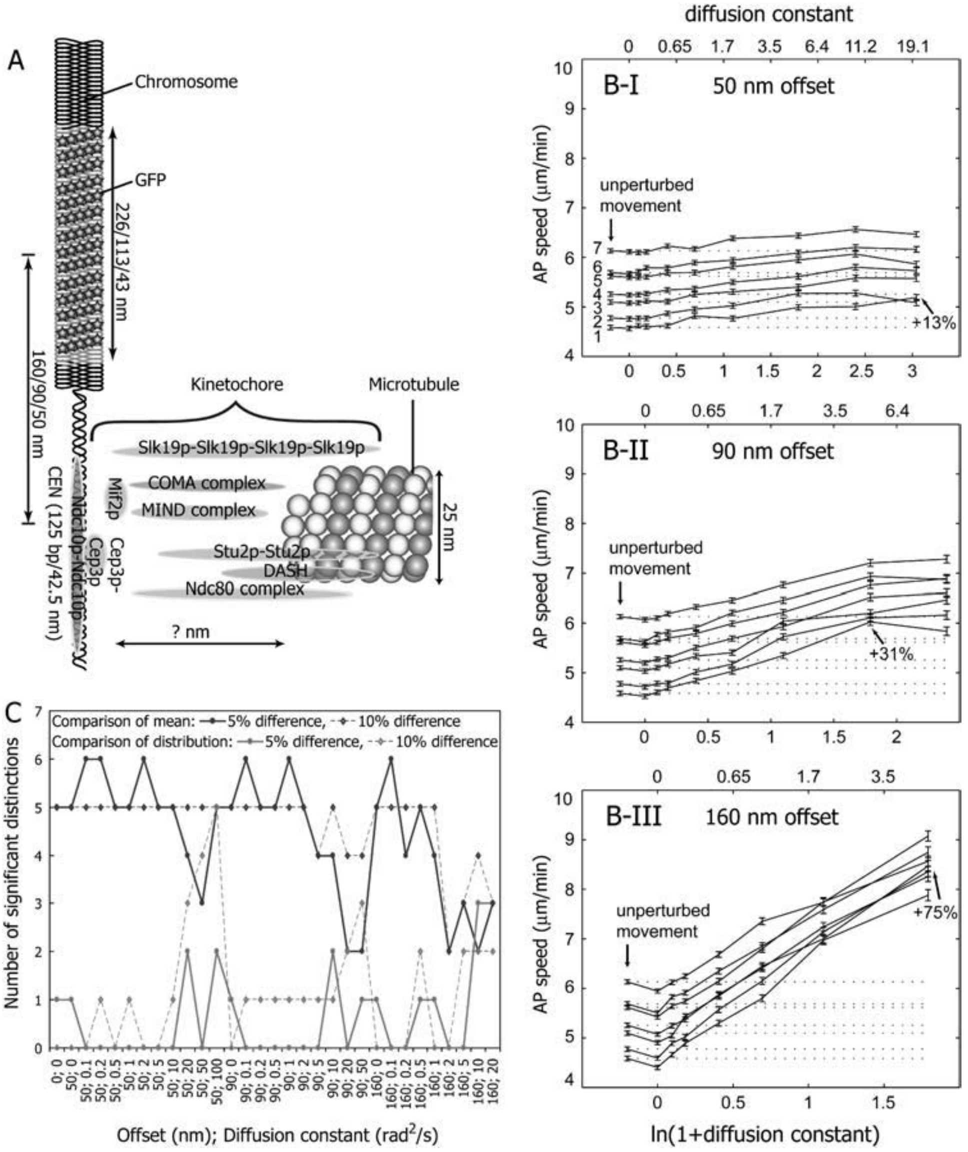

FIGURE 8 Influence of centromere (*CEN*) tag offset from the kinetochore on trajectory analysis. (*A*) Schematic drawing of the position of the centromere marker (after De Wulf et al. (1)). The offset of the tag center from the kinetochore depends on the compaction of yeast G1 chromosomes. (*B*) Influence of rotational diffusion of the CEN tag about the kinetochore on antipoleward (*AP*) speeds for tag offsets of (*I*) 50 nm, (*II*) 90 nm, and (*III*) 160 nm. Seven rates of tubulin association during growth are considered, incrementing in steps of 5% between indices. Arrows indicate the maximum deviation of the speeds from their values without offset (first data point for every sequence) among all seven simulations. (*C*) Distinguishability of trajectories as a function of tag offset and rotational diffusion constant. Dark gray curves display the number of simulation pairs with a difference in the association rate of 5% (*solid line*) and 10% (*dashed line*) that can be distinguished by comparison of the means of the AP speeds. The number of distinguishable pairs decreases with increasing offset and diffusion constant. Light gray curves show the number of 5% increment (*solid line*) and 10% increment (*dashed line*) pairs with differing speed distributions. The higher the influence of the diffusing offset, the stronger the difference of the speed distribution.

significantly for offsets of 50 and 90 nm, which correspond to G1 chromosome compactions of 30- and 80-fold. The observed distance between the CEN tag and the SPB tag is a good approximation of the length of the attached k-MT and the observed motion reflects that of plus-end dynamics. Furthermore, even though trajectory characteristics are influenced by tag rotation about the CEN, the trajectory descriptors do retain their sensitivity and are suitable reporters of the underlying MT dynamics.

### 3D analysis is required to distinguish between phenotypes

In view of the complications posed by tracking of low SNR images of partially overlapping tags, we investigated the possibility of acquiring only one slice per frame, or at least limiting the image analysis to two-dimensional (2D) maximum projections. Although tag localization is clearly simpler in 2D images, resolution is significantly reduced because of information loss in the axial direction. As an extreme example, it is obvious that two tags that are well separated along the *z* axis fuse completely upon the projection onto the *xy*-plane. As indicated in Figs. 1, *C-I–C-III*, and 4 *A*, the SPB-CEN axes often have significant axial components, so that a projection onto the imaging plane obscures tag separation in many cases. More importantly, however, neglecting the axial component of the motion alters the SPB-CEN distance trajectories from which the descriptors of chromosome dynamics are calculated. One approach that has been applied previously to alleviate this problem, which also allows faster imaging, is to acquire only a single slice per frame and to analyze only frames where both tags are in focus (45). This decreases the effect of the neglected axial component, but at the same time reduces the number of valid frames, and thus the effective sampling rate and sample size. Also, this requires very accurate focus adjustment during the very short time between consecutive frames.

We analyzed the effect of axial information loss on SPB-CEN distance trajectory descriptors, by i), projecting 3D coordinates from our 3D data sets onto the imaging plane for all frames, and ii), retaining the projections of only those frames in which both tag signals were visible in the imaging plane. We considered a tag to be visible in the imaging plane if the component of its signal in the imaging plane was at least twice as strong as background noise. Two tags with $SNR = 8$ on opposite sides of the focal plane are therefore both visible in the same plane when they are separated by at most $2\sigma_z\sqrt{-\ln(2/8)} \cong 629\,\text{nm}$, where $\sigma_z$ denotes the half-width of the Gaussian approximating the PSF of a 1.4 N.A. objective lens (15).

Fig. 9 *A* compares the original SPB-CEN distance trajectory from an *ndc10-1* mutant (*black*) to trajectories obtained by maximum projection (*light gray*) or by retaining only frames with in-focus tag pairs (*dark gray*). Trajectories obtained from 2D data markedly differ from the true 3D trajectory. The trajectory constructed from in-focus slices followed the maximum projection trajectory as long as the axial distance between the tags was <629 nm. Toward the end of the movie the tags moved out of the in-focus slice, resulting in the elimination of almost 50% of the data points. This particular trajectory was an extreme case, however, as there is no MT tethering of chromosomes in *ndc10-1* mutant cells. In the examples in Fig. 9 *B*, which compares AP speed of WT with and without benomyl, and *tub2-150* with and without benomyl, the overall rate of data loss was ~10%. Interestingly, data loss made the difference between the AP speed discrimination matrices from in-focus and maximum projection data larger than that between the AP speed discrimination matrices from maximum projection and 3D data. Although AP speed distributions were distinguished similarly in all three trajectory types, significance levels for the comparison of average AP speeds changed. Out of the six pairwise comparisons, maximum projection significance levels differed from those in 3D in four cases, whereas in-focus levels differed in five. Remarkably, both 2D analyses failed to distinguish between AP speeds of WT with and without benomyl.

In conclusion, 2D data analysis leads to significant information loss that can cause severe misinterpretation of phenotypes.

## Fast sampling is required to distinguish between phenotypes

The unique possibility provided by budding yeast to study the dynamics of single k-MTs brings with it the downsides of high dynamics. Very fast sampling is required to capture the true motion. Preliminary simulation results indicate that we need a sampling rate of at least 10 frames per second to avoid aliasing (data not shown). With the requirement for 3D sampling, this would lead to exposure times of ~5 ms (instead of the current 35-ms exposures) per z-slice per 3D frame of 16 z-slices. Such image acquisition rates are not realistic considering the low photostability of the GFP tags as well as the finite photon sensitivity and rate-dependent readout noise of the available charge-coupled device detectors. Therefore, we had to find a trade-off between temporal undersampling of MT dynamics and the SNR of the tag that defined our ability to track the signals over sufficient time windows. The undersampling was accompanied by significant underestimation of the speeds and switching frequencies, which monotonically decrease with the sampling rate (33). As with tag offset, sampling-dependent alterations in absolute speeds are not critical as long as their sensitivity in distinguishing between phenotypes is conserved and phenotypes are only compared based on equally sampled data. However, Monte Carlo simulations of MT dynamics indicated to us that the sensitivity of AP and TP speeds, as well as switching frequencies, was rapidly lost with decreasing sampling rate (data not shown).

We validated the simulation results by artificially downsampling our experimental data. For instance, to generate

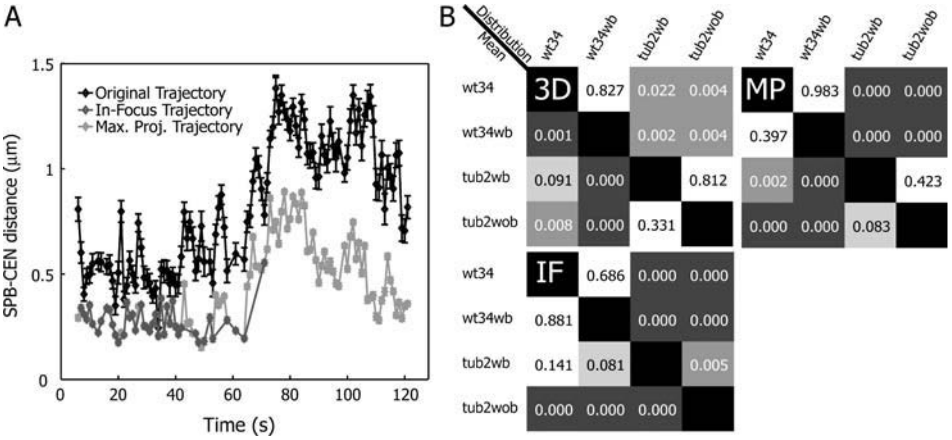

FIGURE 9 Analysis of kinetochore microtubule dynamics in yeast requires 3D imaging. (*A*) SPB-CEN distance trajectory calculated from complete 3D tracks (*black*); from tracks generated by maximum projection of image data onto the *xy*-plane (*light gray*); and from tracks sampled in frames containing both tag signals in the same plane in focus (*dark gray*). (*B*) Discrimination matrices for the comparison of AP speed of 3D and 2D trajectories of WT and *tub2-150* at 34°C with and without benomyl. Two-dimensional trajectories modify the significance levels of mean speed and speed distribution discrimination substantially. See Fig. 7 for gray level codes and abbreviations.

data sampled at 2 s from data sampled at 1 s, while conserving the total number of data points, we split every 1-s SPB-CEN distance trajectory into two trajectories, each consisting of alternating time points from the original trajectory. A sampling rate of 10 s instead of 1 s turned out to reduce the AP speed by a factor four (Fig. 10 *A*). The ability to distinguish between phenotypes generally decreased as the sampling rate decreased. Fig. 10 *B* displays how the discrimination matrices change with undersampling for the phenotypes of WT and *tub2-150* at 34°C, each with and without benomyl. The most dramatic loss of sensitivity occurs between WT with and without benomyl, whose mean velocities were indistinguishable already at 3-s sampling. By contrast, the differences between *tub2-150* and the other conditions increased with undersampling. This might indicate that AP and TP speeds as descriptors of MT dynamics fail to capture an important property of the *tub2-150* phenotype.

In summary, although our frame rate of 1/s seems to significantly alias k-MT dynamics in yeast, AP and TP offer in most cases statistically distinguishable descriptors for different phenotypes. The sensitivity of these descriptors steeply decreases when sampling falls below 1/3 $s^{-1}$.

## A large amount of data is required to characterize phenotypes

We examined how much data we needed for AP and TP speeds as descriptors of MT dynamics to converge to unique values for a specific phenotype. The results for WT at 37°C are shown in Fig. 11. To construct convergence graphs, we acquired 50 movies and assembled their distance trajectories in an arbitrary sequence to estimate AP and TP statistics with an increasing number of movies included in the analysis. This procedure was repeated for 10 random permutations of trajectory orders. In all permutations, we found that AP and TP speeds converged to stable values when ~350 events of each AP and TP motion were used. This translated into a requirement of 20–25 movies, or ~2000 data points, for reliable characterization of each phenotype, as one movie contains on average 18 events of AP or TP motion.

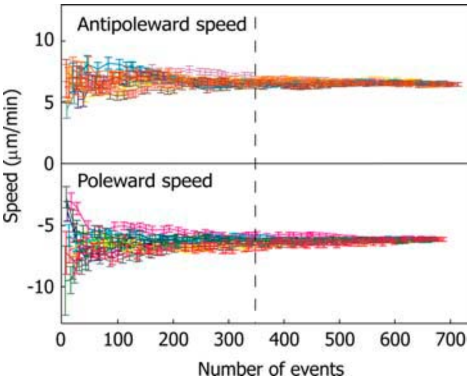

FIGURE 11 Convergence of estimated antipoleward and poleward speeds for WT at 37°C as a function of the number of data points. Colors refer to 10 randomly permuted trajectory sequences. At least 350 events of AP or TP motion are required to estimate stable AP or TP speeds (*vertical dashed line*). On average, a trajectory of 100 s, sampled at 1 s, contains 18 events of AP and TP movement. Therefore, 20–25 movies are required per condition to characterize its phenotype in microtubule dynamics.

## Centromere and SPB are never closer than ~200 nm

Of the >20,000 SPB-CEN distances considered in this article, only two are smaller than 200 nm (196 and 197 nm in Fig. 5 *B*). This corresponds to 85% of the inverse of the OTF frequency cutoff in the direction the SPB-CEN axis was observed in these data points. However, in other data points we measured distances at 75% of the inverted OTF cutoff. Assuming that all SPB-CEN axis orientations are equally likely, data along an equiresolution line (*horizontal lines* in Fig. 5 *B*) should be distributed in a ratio of 8:3:2:1 for axis orientations of 0–22.5°, 22.5–45°, 45–67.5°, and 67.5–90°, respectively. Instead, the domain 0–30°, in which a resolution of 75% of the inverted OTF cutoff would allow us to observe distances between 170 and 200 nm, is devoid of data points

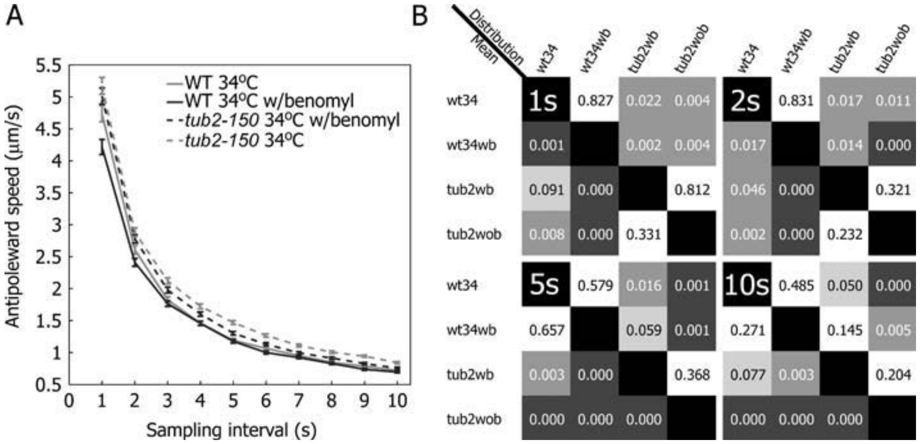

| Distribution / Mean | wt34 | wt34wb | tub2wb | tub2wob | wt34 | wt34wb | tub2wb | tub2wob |
|---|---|---|---|---|---|---|---|---|
| wt34 | 1s | 0.827 | 0.022 | 0.004 | 2s | 0.831 | 0.017 | 0.011 |
| wt34wb | 0.001 |  | 0.002 | 0.004 | 0.017 |  | 0.014 | 0.000 |
| tub2wb | 0.091 | 0.000 |  | 0.812 | 0.046 | 0.000 |  | 0.321 |
| tub2wob | 0.008 | 0.000 | 0.331 |  | 0.002 | 0.000 | 0.232 |  |
| wt34 | 5s | 0.579 | 0.016 | 0.001 | 10s | 0.485 | 0.050 | 0.000 |
| wt34wb | 0.657 |  | 0.059 | 0.001 | 0.271 |  | 0.145 | 0.005 |
| tub2wb | 0.003 | 0.000 |  | 0.368 | 0.077 | 0.003 |  | 0.204 |
| tub2wob | 0.000 | 0.000 | 0.000 |  | 0.000 | 0.000 | 0.000 |  |

FIGURE 10 Influence of the frame rate on antipoleward speed. (*A*) AP speeds strongly diminish with undersampling. Speeds were extracted by artificially subsampling experimental data acquired at a frame rate of 1/s on WT and *tub2-150* at 34°C, with and without benomyl. (*B*) Discrimination matrix of AP speeds at 1-, 2-, 5-, and 10-s sampling intervals. With the exception of *tub2-150* without benomyl, the sensitivity in distinguishing different strains and conditions decreases with lower sampling rates. See Fig. 7 for gray level codes and abbreviations.

(*blue shaded triangle* in Fig. 5). This suggests that the absence of distances shorter than 200 nm has a biological rather than a technical basis.

As shown in Fig. 12, the first 120 nm of the minimum distance probably reflect the size of the SPB and the k-MT. According to an electron microscopy study (9), the distance between the location of Spc42p, i.e., our SPB tag, and the MT nucleation site is ~70 nm, and the shortest interphase nuclear MTs are ~50-nm long. The remaining 80 nm are due to the size of the kinetochore and the offset of the CEN tag. To maximize the possible effect of the offset of the CEN tag, we assumed that the kinetochore did not extend between chromosome and MT tip, i.e., that the MT directly touched the chromosome. Fig. 12 *A* shows the angles that offsets of 50, 90, and 160 nm make with the MT axis. The latter two make angles of 36 and 90°, respectively, with a zero-length kinetochore. The 50-nm offset, even when perfectly aligned with the MT axis, requires a kinetochore that is at least 30-nm long.

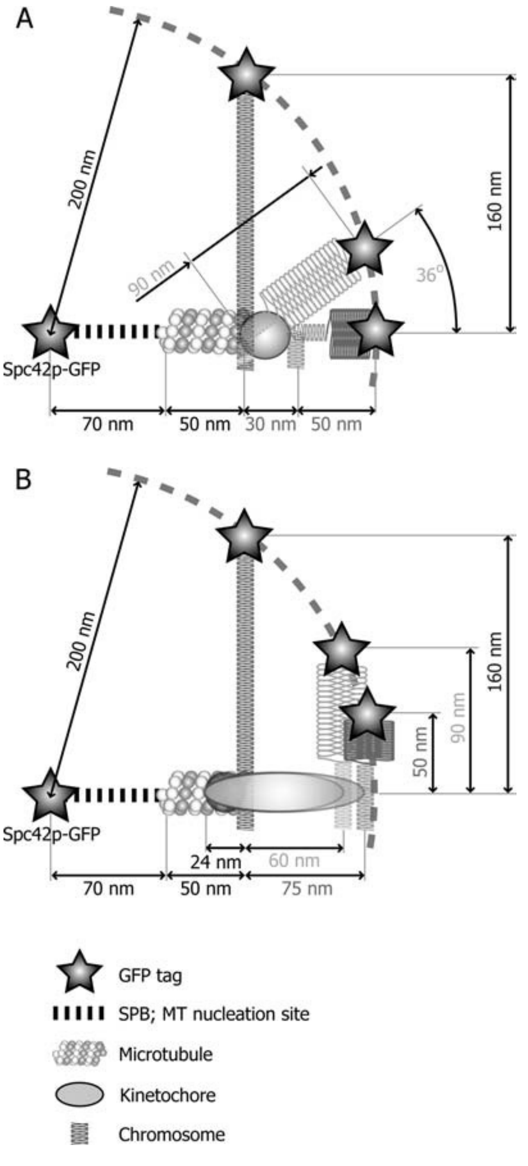

FIGURE 12 Models for the geometric configurations of SPB and CEN tags near the 200-nm minimum distance. The distance between the GFP-tagged Spc42p and MT nucleation site is ~70 nm, and the shortest MT in the yeast interphase nucleus is ~50 nm. (*A*) Configuration with a kinetochore of length 0. The minimum distance of 200 nm can be explained by CEN tag offsets with angles between chromosome arm and MT axis of 90 and 36° for offsets of 160 and 90 nm, respectively. An offset of 50 nm requires a minimum kinetochore length of 30 nm. (*B*) Configuration with a mean angle between chromosome arm and MT axis of 90°. Assuming a kinetochore-to-MT overlap of three dimer layers, the length of the kinetochore is estimated to be 25, 85, and 100 nm for offsets of 160, 90, and 50 nm, respectively.

However, the assumption of zero kinetochore extension is unrealistic (1). In addition, our data show that chromosomes of *ndc10-1* can diffuse almost as close to the SPB as WT chromosomes pulled by MTs (see Table 1). It is therefore unlikely that the density of material around the SPB is so high that chromosome arms are always bent away from the pole.

Hence, we investigated a more probable configuration assuming that the CEN proximal chromatin forms a right angle with the MT axis and that the kinetochore overlaps with the MT for three dimer layers (24 nm); Fig. 12 *B* shows the estimated length of the kinetochore that would account for the extra 80 nm. The 50 and 90 nm offsets yield kinetochore lengths of ~100 nm (24 + 75 nm) and ~85 nm (24 + 60 nm), which are compatible with the elongated structures of the kinetochore complexes proposed previously (1). The zero kinetochore extension for the 160-nm offset makes this configuration again unlikely, and indicates that G1 chromosome compaction must be higher than our most conservative assumption of 15-fold.

In summary, we conclude that the measured minimum SPB-CEN distance of 200 nm is due neither to limits in the resolution achieved by our algorithms, nor solely to the tag offset. Based on a simple geometric model of the MT and chromosome arrangement we infer that the kinetochore may be as long as ~85–100 nm. This will have to be confirmed in the future based on structural analysis of the kinetochore proteins.

## Chromosomes are attached to MTs via kinetochores in G1 and exhibit directional instability

In G1, the confinement volume of the CEN-proximal region in *ndc10-1*, where there is no functional kinetochore and hence no MT attachment, was found to be ~13 times greater than in any other strain and condition we investigated. A similar increase in confinement volume upon detachment, induced by prolonged exposure to nocodazole, was observed by Marshall et al. (35) for two tags placed 22 kb from the centromere in diploid yeast cells. In addition, WT and *tub2-150*, but not *ndc10-1*, chromosomes showed significant changes in dynamics upon application of benomyl.

We therefore conclude that chromosomes are attached to MTs in G1, and that their movement is dependent on k-MT dynamics. Although we cannot fully rule out the possibility of chromosomes attaching to the side of MTs, this possibility seems very unlikely as the dynamics change with benomyl exposure and the tubulin mutation *tub2-150*, which are both known to specifically affect MT tip dynamics. Furthermore, because CEN tags sampled a larger volume and moved significantly faster in *ndc10-1* cells than in strains with k-MT attachment, we purport that the chromosome is long and flexible enough so that chromosome tethering to the nuclear membrane does not have a long-range effect on CEN motion. Thus, we propose our method as a sensitive assay for probing the molecular regulation of k-MT plus-end dynamics in G1.

## K-MTs and cytoplasmic MTs are regulated by distinct mechanisms

With the exception of *tub2-150* cells in the absence of benomyl, all strains and conditions we investigated exhibited the same mean AP and TP speeds. This contrasts with data on cytoplasmic MTs that are observed to shrink faster than they grow (Table 2). To make our data as comparable as possible to the cited references we artificially downsampled our trajectories to a frame rate of 1/10 per second. At this sampling rate, the speeds of cytoplasmic and kinetochore MTs were of comparable magnitude. However, the switching frequencies of k-MTs were an order of magnitude larger than those of cytoplasmic MTs. These results indicate that k-MTs and cytoplasmic MTs are differentially regulated.

## Low temperature and benomyl attenuate kinetochore MT dynamics

MT dynamics has hitherto been analyzed mainly by mean values of speeds and switching frequencies. Although it is known that MT growth and shrinkage speeds are intrinsically variable (46), their distributions have never been used to discriminate phenotypes in cells. However, our simulations indicated that when there is a fundamental change in the type of motion that the centromere tag describes, e.g., when the rotational diffusion of the tag about the kinetochore becomes the dominant contribution to the motion, the speed distributions, rather than the mean speeds, change (Fig. 8 *C*). From this, we conjecture that changes in distributions are indicative of fundamental changes in the system, such as the activation or silencing of regulatory pathways, whereas changes in only mean speeds are indicative of adjustments in the equilibrium state of the system within one regulatory regime.

MTs tend to depolymerize at low temperatures (47,48). Accordingly, one would expect that increasingly lower temperatures shift the equilibrium concentrations toward shorter MTs and larger pools of free tubulin dimers. This is confirmed by our data where we observed shorter average SPB-CEN distances at reduced temperatures. Lower temperatures also diminished both AP and TP speeds in a nonlinear fashion (cf. Table 1); averages of both speeds and average distance decreased by about twice as much from 37 to 34°C as compared to the decrease from 34 to 25°C. Arrhenius-like temperature dependence of the rate of tubulin addition has been estimated from in vitro experiments (49). This model describes a nonlinear relationship between temperature decrease and AP speed (assuming that the rate of tubulin addition and AP speed are proportional). In stark contrast to our data, the model predicts the AP speed decrease from 37 to 34°C to be approximately half the decrease from 34 to 25°C. In addition, our experiments indicated that between 37 and 34°C AP and TP speed distributions change significantly, whereas they stay the same between 34 and 25°C. Unlike at any other temperature, the distributions of AP and TP speeds were different at 37°C. These temperature dependences cannot be easily explained by thermodynamic equilibrium shifts in MT polymerization kinetics alone, but suggest that changes in k-MT dynamics between 34 and 37°C are associated with differential regulation. We currently investigate the specific roles of heat shock responses at 37°C as a possible mechanism causing the significant change in motion type (50). These data further support our speculation that differences in speed distributions between phenotypes originate from differential regulation, whereas phenotypes where only the mean speeds differ, but not the distributions, are associated with shifts of the thermodynamic equilibrium within one regulatory regime.

The fungicide benomyl binds to tubulin dimers, and has been observed to prevent MT assembly at high concentrations both in vitro and in vivo (51–53). However, yeast nuclear MTs seem to be resistant to depolymerization at fairly high benomyl concentrations (80 $\mu$g/ml) (54). We have found that exposure of cells to 40 $\mu$g/ml benomyl indeed do not lead to the disappearance of MTs in WT cells. Instead, we observed that average SPB-CEN distance shortened, and both AP and TP movements of the chromosome

**TABLE 2 Comparison of WT budding yeast cytoplasmic and kinetochore MT dynamics in G1**

| Source | Growth speed ($\mu$m/min) | Shrinkage speed ($\mu$m/min) | Catastrophe frequency (1/s) | Rescue frequency (1/s) | Sampling interval (s) | Temperature (°C) |
|---|---|---|---|---|---|---|
| Carminati and Steams, 1997 (60) | 0.51 ± 0.047 (14) | 1.784 ± 0.19 (11) | 0.007 (10) | – | 2 or 10 | Room temperature |
| Tirnauer et al., 1999 (45) | 2.17 ± 0.26 (38) | 3.2 ± 0.24 (33) | 0.008 (30) | 0.007 (24) | 8 | 23 |
| Kosco et al., 2001 (34) | 0.79 ± 0.38 (17) | 1.55 ± 1.08 (20) | 0.007 (20) | 0.006 (13) | 10 or 20 | 23 |
| Gupta et al., 2002 (61) | 1.66 ± 0.54 (31) | 2.66 ± 0.77 (34) | 0.009 ± 0.002 (28) | 0.004 ± 0.002 (14) | 8 | 23 |
| WT25, this study | 0.65 ± 0.02 (610) | 0.67 ± 0.02 (523) | 0.074 ± 0.002 (508) | 0.078 ± 0.002 (473) | 10 | 25 |

K-MT dynamics have been calculated from artificially downsampled trajectories.

slowed down. The distributions of AP and TP speeds of WT with benomyl at 34°C are not different from WT without benomyl at 34 and 25°C. It has been reported previously that low concentrations of MT destabilizing drugs, such as nocodazole or benomyl, can attenuate MT dynamics in vitro and in vivo (55). The effect has also been shown for microtubules of the yeast mitotic spindle (55,56).

Interestingly, our results suggest that the attenuation of k-MT dynamics caused by benomyl at 34°C is similar to the attenuation caused by a temperature shift from 34 to 25°C, and that neither is accompanied by a major alteration of k-MT dynamics regulation.

At 37°C, exposure of WT cells to benomyl has again an effect similar to lowering the temperature. AP and TP speeds are reduced to levels between 25 and 34°C, and speed distributions are more similar to those of WT at 34°C. The overall much stronger effect of benomyl on AP and TP speeds at 37°C as compared to 34°C could be due to either differential regulation of k-MT dynamics at 37°C, as suggested above, or it could be due to a faster metabolization of benomyl at 37°C, leading to a higher effective benomyl concentration.

### MT dynamics are increased in the tubulin mutant *tub2-150*

*Tub2-150*, a mutant in the budding yeast $\beta$-tubulin, was discovered in screens for benomyl-resistant tubulin mutants (57). Under nonpermissive conditions (withdrawal of benomyl at 34°C), the mutant perishes due to nuclear mislocalization, which indicates a misregulation of MT dynamics. One way to rescue *tub2-150* cells is by exposing them to benomyl, which caused the mutant to be designated as depolymerization inhibited (58,59).

As expected, we found that 40 $\mu$g/ml of benomyl set AP and TP speeds in *tub2-150* back to their WT values. The only significant difference between the speeds of *tub2-150* with benomyl and WT at 34°C was in the distribution of AP speeds. In the absence of benomyl, we found that TP motion in *tub2-150* is significantly faster than in WT or under permissive conditions, whereas the AP motion was not affected. We therefore conclude that benomyl rescues *tub2-150* cells because it attenuates their faster depolymerization dynamics, and not because it makes hyperstable MTs depolymerize.

Interestingly, *tub2-150* is not only rescued by benomyl, but also by temperature shifts below 26°C (57). This is consistent with the similarity between the attenuation of MT dynamics by benomyl exposure and temperature decrease.

## CONCLUSION

Here we report for the first time single kinetochore-MT dynamics in budding yeast. Comparing chromosome dynamics of *ndc10-1* mutants to WT, we have confirmed that chromosomes are attached in the G1 phase of the cell cycle, which allows us to directly monitor and analyze single k-MT dynamics in budding yeast nuclei. To examine the sensitivity of our assay in distinguishing between weak phenotypes, we have studied the effect of temperature, exposure to benomyl, and a tubulin mutation on k-MT dynamics. We have found that lowering the temperature and exposure to benomyl both attenuate k-MT dynamics in a similar manner, and that the mutant *tub2-150* does not form hyperstable MTs as described previously, but that the mutation significantly increases both MT growth and shrinkage rates.

To follow chromosome dynamics, we tagged the SPB and chromosome IV at 1.1 kb from the centromere with GFP. Using simulations we have shown that this tag offset does not obscure MT dynamics. We further demonstrated that to sensitively measure MT dynamics, we needed 1-s sampling, 3D imaging, and image analysis capable of distinguishing tags at low SNR that are separated by less than the inverse of the frequency cutoff of the microscope's optical transfer function.

Based on these findings, we propose our assay as a powerful tool for the study of the chemical and mechanical regulation of single k-MT dynamics by kinetochore and other MT binding proteins.

## APPENDIX

The 10-kb GFP tag reporting the position of the kinetochore was placed 1.1 kb off the CEN region (as shown in Fig. 8 *A*), rendering the detected motion of the CEN tag a superposition of the motion of the CEN region as driven by the dynamic instability of the attached k-MT and the thermal motion of the tag relative to the CEN. The extent to which the latter contributed to the overall observed motion was a critical issue that we analyzed using the theoretical arguments and simulations described here.

Our model of MT dynamics considered an MT to be a linear polymer of 13-tubulin-ring units. The MT polymerized and depolymerized via a competition between rates of unit addition, loss, and hydrolysis. Rates of unit addition and loss had different values during growth and shrinkage, whereas the rate of addition during growth and the rate of loss during shrinkage were MT-length dependent as well (40). Model parameters were adjusted to produce dynamics that resembled those observed experimentally for WT yeast in G1.

The motion of the tag relative to the CEN was considered to be a damped rotation, where the distance between the tag and the CEN was held fixed, and was modeled as a random walk in a two-dimensional angular space. Simulating the rotational diffusion of the tag about the kinetochore required two parameters: the geometrical distance between the tag and the CEN, which depended on the packing of interphase yeast chromosomes, and the rotational diffusion constant of the tag. Because there were no established experimental measurements of the compaction ratio, shape, or rotational diffusion constant of these chromosomes, we reasoned about the magnitudes of the required parameters.

The distance between tag and CEN, referred to as offset hereafter, was calculated as

$$(125/2\,\mathrm{bp}) \times (0.34\,\mathrm{nm/bp}) + ((1.1 + 10/2)\mathrm{kb}) \\ \times (340\,\mathrm{nm/kb})/\alpha.$$

The first term accounted for half the length of the CEN region, which was assumed to be in naked DNA form (0.34 nm/bp), whereas the second term accounted for the distance between CEN edge and tag center, which was assumed to be $\alpha$-fold compacted. Under the assumption that the CEN region was completely rigid due to kinetochore attachment, the first term in the above equation could be neglected, reducing the offset by ~20 nm. Nevertheless, we retained this term to study the worst possible case.

There were several possible values for the compaction ratio. Due to the fact that the CEN tag image never exceeded the size of the point spread function, we inferred that the tag was at the very most 228.75-nm long, corresponding to the lateral resolution limit of the microscope. This yielded a compaction ratio of $\sim(340\,\text{nm/kb})/(228.75\,\text{nm}/10\,\text{kb}) \approx 15$. Another value for the compaction ratio arose from the assumption that interphase yeast chromosomes had the 30-nm chromatin fiber structure, in which case they would be ~30-fold compacted (41). A third possible value was the 80-fold compaction determined by Guacci et al. (44) using fluorescence in situ hybridization. Compactions (15-, 30- and 80-fold) resulted in an offset of 160, 90, and 50 nm, respectively.

As for the tag's rotational diffusion constant, we tuned it to obtain simulated trajectories that, like experimental trajectories, spent 20–30% of the time in growth phase, 20–30% in shrinkage phase, and ~10% in pause (whereas 30–40% of the trajectory remained undetermined), as shown in Table 1. Because trajectories tended to spend more time in pause and to have more undetermined intervals with increasing diffusion constant, this criterion yielded maximum diffusion constants of ~20 rad$^2$/s, ~10 rad$^2$/s, and ~5 rad$^2$/s for offsets of 50, 90, and 160 nm, respectively. These diffusion constants are very large (a diffusion constant of 10 rad$^2$/s produces a rotation of ~256° in 1 s), accounting for the maximum possible effect of tag rotation on the observed motion. Notice, however, that our criterion ruled out free tag rotation, which resulted in too much pause and undetermined trajectory segments.

Using the above MT dynamics and rotational diffusion models, detailed trajectories of both the MT tip (which coincided with the position of the CEN) and the tag were obtained by Monte Carlo simulations. The simulation time step was taken to be small enough to capture every event of unit association, dissociation, and hydrolysis, as well as to allow the tag to rotate about the MT tip in small steps. These trajectories were averaged over 1-s intervals, yielding average positions and standard deviations at experimental observation times.

## SUPPLEMENTARY MATERIAL

An online supplement to this article can be found by visiting BJ Online at http://www.biophysj.org.

This work was funded by a fellowship from the Roche Research Foundation to J.F.D, and by National Institutes of Health grant GM 68956 to P.K.S. and G.D. K.J. is a Paul Sigler/Agouron fellow of the Helen Hay Whitney Foundation. TSRI MS No. 17132-CB.

## REFERENCES

1. De Wulf, P., A. D. McAinsh, and P. K. Sorger. 2003. Hierarchical assembly of the budding yeast kinetochore from multiple subcomplexes. *Genes Dev.* 17:2902–2921.
2. McAinsh, A. D., J. D. Tytell, and P. K. Sorger. 2003. Structure, function, and regulation of budding yeast kinetochores. *Annu. Rev. Cell Dev. Biol.* 19:519–539.
3. Mitchison, T., and M. Kirschner. 1984. Dynamic instability of microtubule growth. *Nature.* 312:237–242.
4. Kinoshita, K., I. Arnal, A. Desai, D. N. Drechsel, and A. A. Hyman. 2001. Reconstitution of physiological microtubule dynamics using purified components. *Science.* 294:1340–1343.
5. Janson, M. E., M. E. de Dood, and M. Dogterom. 2003. Dynamic instability of microtubules is regulated by force. *J. Cell Biol.* 161: 1029–1034.
6. He, X., S. Asthana, and P. Sorger. 2000. Transient sister chromatid separation and elastic deformation of chromosomes during mitosis in budding yeast. *Cell.* 101:763–775.
7. Pearson, C. G., P. S. Maddox, E. D. Salmon, and K. Bloom. 2001. Budding yeast chromosome structure and dynamics during mitosis. *J. Cell Biol.* 152:1255–1266.
8. Winey, M., C. Mamay, E. O'Toole, D. Mastronarde, T. Giddings, Jr., K. McDonald, and J. McIntosh. 1995. Three-dimensional ultrastructural analysis of the Saccharomyces cerevisiae mitotic spindle. *J. Cell Biol.* 129:1601–1615.
9. O'Toole, E. T., M. Winey, and J. R. McIntosh. 1999. High-voltage electron tomography of spindle pole bodies and early mitotic spindles in the yeast Saccharomyces cerevisiae. *Mol. Biol. Cell.* 10:2017–2031.
10. Maddox, P. S., K. S. Bloom, and E. D. Salmon. 2000. The polarity and dynamics of microtubule assembly in the budding yeast Saccharomyces cerevisiae. *Nat. Cell Biol.* 2:36–41.
11. Cheeseman, I. M., C. Brew, M. Wolyniak, A. Desai, S. Anderson, N. Muster, J. R. Yates, T. C. Huffaker, D. G. Drubin, and G. Barnes. 2001. Implication of a novel multiprotein Dam1p complex in outer kinetochore function. *J. Cell Biol.* 155:1137–1145.
12. Westermann, S., I. M. Cheeseman, S. Anderson, J. R. Yates III, D. G. Drubin, and G. Barnes. 2003. Architecture of the budding yeast kinetochore reveals a conserved molecular core. *J. Cell Biol.* 163:215–222.
13. He, X. W., D. R. Rines, C. W. Espelin, and P. K. Sorger. 2001. Molecular analysis of kinetochore-microtubule attachment in budding yeast. *Cell.* 106:195–206.
14. Straight, A. F., A. S. Belmont, C. C. Robinett, and A. W. Murray. 1996. GFP tagging of budding yeast chromosomes reveals that protein-protein interactions can mediate sister chromatid cohesion. *Curr. Biol.* 6:1599–1608.
15. Thomann, D., D. R. Rines, P. K. Sorger, and G. Danuser. 2002. Automatic fluorescent tag detection in 3D with super-resolution: application to the analysis of chromosome movement. *J. Microsc.* 208: 49–64.
16. Thomann, D., J. Dorn, P. K. Sorger, and G. Danuser. 2003. Automatic fluorescent tag localization II: improvement in super-resolution by relative tracking. *J. Microsc.* 211:230–248.
17. Mitchison, T. J., and E. D. Salmon. 2001. Mitosis: a history of division. *Nat. Cell Biol.* 3:E17–E21.
18. Jin, Q. W., J. Fuchs, and J. Loidl. 2000. Centromere clustering is a major determinant of yeast interphase nuclear organization. *J. Cell Sci.* 113:1903–1912.
19. Winey, M., and E. T. O'Toole. 2001. The spindle cycle in budding yeast. *Nat. Cell Biol.* 3:E23–E27.
20. Heun, P., T. Laroche, K. Shimada, P. Furrer, and S. M. Gasser. 2001. Chromosome dynamics in the yeast interphase nucleus. *Science.* 294: 2181–2186.
21. Robinow, C., and J. Marak. 1966. A fiber apparatus in the nucleus of the yeast cell. *J. Cell Biol.* 29:129–151.
22. Goh, P. Y., and J. V. Kilmartin. 1993. Ndc10: a gene involved in chromosome segregation in Saccharomyces-cerevisiae. *J. Cell Biol.* 121:503–512.
23. Hyman, A. A., and P. K. Sorger. 1995. Structure and function of kinetochores in budding yeast. *Annu. Rev. Cell Dev. Biol.* 11:471–495.
24. Danuser, G. 2001. Super-resolution microscopy using normal flow decoding and geometric constraints. *J. Microsc.* 204:136–149.
25. Rines, D. R., X. W. He, and P. K. Sorger. 2002. Quantitative microscopy of green fluorescent protein-labeled yeast. *In* Guide to Yeast Genetics and Molecular Biology. C. Guthrie and G. R. Fink, editors. Academic Press. San Diego, CA. 16–34.
26. Rines, D., D. Thomann, J. Dorn, P. Goodwin, and P. Sorger. 2004. Live cell imaging of yeast. *In* Live Cell Imaging: A Laboratory Manual. R. D. Goldman and D. L. Spector, editors. Cold Spring Harbor Laboratory Press, Woodbury, NY. 631.
27. Pask, C. 1975. Simple optical theory of super-resolution. *J. Opt. Soc. Am.* 66:68–70.

28. Cox, I. J., and C. J. R. Sheppard. 1986. Information capacity and resolution in an optical-system. *J. Opt. Soc. Am. A Opt. Image Sci. Vis.* 3:1152–1158.

29. Koch, K.-R. 1988. Parameter Estimation and Hypothesis Testing in Linear Models. Springer-Verlag, Berlin/Heidelberg, Germany.

30. Saxton, M. J. 1997. Single-particle tracking: the distribution of diffusion coefficients. *Biophys. J.* 72:1744–1753.

31. Saxton, M. J. 1993. Lateral diffusion in an archipelago: single-particle diffusion. *Biophys. J.* 64:1766–1780.

32. Skibbens, R., V. Skeen, and E. Salmon. 1993. Directional instability of kinetochore motility during chromosome congression and segregation in mitotic newt lung cells: a push-pull mechanism. *J. Cell Biol.* 122:859–875.

33. Shelden, E., and P. Wadsworth. 1993. Observation and quantification of individual microtubule behavior in vivo-microtubule dynamics are cell-type specific. *J. Cell Biol.* 120:935–945.

34. Kosco, K. A., C. G. Pearson, P. S. Maddox, P. J. J. Wang, I. R. Adams, E. D. Salmon, K. Bloom, and T. C. Huffaker. 2001. Control of microtubule dynamics by Stu2p is essential for spindle orientation and metaphase chromosome alignment in yeast. *Mol. Biol. Cell.* 12:2870–2880.

35. Marshall, W., A. F. Straight, J. F. Marko, J. Swedlow, A. Dernburg, A. S. Belmont, A. Murray, D. Agard, and J. W. Sedat. 1997. Interphase chromosomes undergo constrained diffusional motion in living cells. *Curr. Biol.* 7:930–939.

36. Goodman, J. W. 1968. Introduction to Fourier Optics. McGraw-Hill, New York, NY.

37. Carrington, W. A., R. M. Lynch, E. D. W. Moore, G. Isenberg, K. E. Fogarty, and F. S. Fredric. 1995. Super-resolution 3-dimensional images of fluorescence in cells with minimal light exposure. *Science.* 268:1483–1487.

38. Toraldo di Francia, G. 1955. Resolving power and information. *J. Opt. Soc. Am.* 45:497–501.

39. Sheskin, D. J. 2004. Handbook of Parametric and Nonparametric Statistical Procedures. Chapman and Hall, Boca Raton, FL.

40. Sprague, B. L., C. G. Pearson, P. S. Maddox, K. S. Bloom, E. D. Salmon, and D. J. Odde. 2003. Mechanisms of microtubule-based kinetochore positioning in the yeast metaphase spindle. *Biophys. J.* 84:3529–3546.

41. Gerchman, S. E., and V. Ramakrishnan. 1987. Chromatin higher-order structure studied by neutron-scattering and scanning-transmission electron-microscopy. *Proc. Natl. Acad. Sci. USA.* 84:7802–7806.

42. Dekker, J., K. Rippe, M. Dekker, and N. Kleckner. 2002. Capturing chromosome conformation. *Science.* 295:1306–1311.

43. Bystricky, K., P. Heun, L. Gehlen, J. Langowski, and S. M. Gasser. 2004. Long-range compaction and flexibility of interphase chromatin in budding yeast analyzed by high-resolution imaging techniques. *Proc. Natl. Acad. Sci. USA.* 101:16495–16500.

44. Guacci, V., E. Hogan, and D. Koshland. 1994. Chromosome condensation and sister-chromatid pairing in budding yeast. *J. Cell Biol.* 125:517–530.

45. Tirnauer, J. S., E. O'Toole, L. Berrueta, B. E. Bierer, and D. Pellman. 1999. Yeast Bim1p promotes the G1-specific dynamics of microtubules. *J. Cell Biol.* 145:993–1007.

46. Gildersleeve, R. F., A. R. Cross, K. E. Cullen, A. P. Fagen, and R. C. Williams. 1992. Microtubules grow and shorten at intrinsically variable rates. *J. Biol. Chem.* 267:7995–8006.

47. Inoue, S. 1959. Motility of cilia and the mechanism of mitosis. *Rev. Mod. Phys.* 31:402–408.

48. Inoue, S., and E. D. Salmon. 1995. Force generation by microtubule assembly/disassembly in mitosis and related movements. *Mol. Biol. Cell.* 6:1619–1640.

49. Sept, D., H. J. Limbach, H. Bolterauer, and J. A. Tuszynski. 1999. A chemical kinetics model for microtubule oscillations. *J. Theor. Biol.* 197:77–88.

50. Craig, E. A., and K. Jacobsen. 1984. Mutations of the heat inducible 70-kilodalton genes of yeast confer temperature sensitive growth. *Cell.* 38:841–849.

51. Kilmartin, J. V. 1981. Purification of yeast tubulin by self-assembly in vitro. *Biochemistry.* 20:3629–3633.

52. Albertini, S., M. Brunner, and F. E. Wurgler. 1993. Analysis of the 6 additional chemicals for in vitro assays of the European Economic Communities' EEC aneuploidy program using Saccharomyces cerevisiae D61.M and the in vitro porcine brain tubulin assembly assay. *Environ. Mol. Mutagen.* 21:180–192.

53. Gupta, K., J. Bishop, A. Peck, J. Brown, L. Wilson, and D. Panda. 2004. Antimitotic antifungal compound benomyl inhibits brain microtubule polymerization and dynamics and cancer cell proliferation at mitosis, by binding to a novel site in tubulin. *Biochemistry.* 43:6645–6655.

54. Jacobs, C. W., A. E. M. Adams, P. J. Szaniszlo, and J. R. Pringle. 1988. Functions of microtubules in the Saccharomyces cerevisiae cell cycle. *J. Cell Biol.* 107:1409–1426.

55. Vasquez, R. J., B. Howell, A. M. C. Yvon, P. Wadsworth, and L. Cassimeris. 1997. Nanomolar concentrations of nocodazole alter microtubule dynamic instability in vivo and in vitro. *Mol. Biol. Cell.* 8:973–985.

56. Pearson, C. G., P. S. Maddox, T. R. Zarzar, E. D. Salmon, and K. Bloom. 2003. Yeast kinetochores do not stabilize Stu2p-dependent spindle microtubule dynamics. *Mol. Biol. Cell.* 14:4181–4195.

57. Thomas, J. H., N. F. Neff, and D. Botstein. 1985. Isolation and characterization of mutations in the beta-tubulin gene of Saccharomyces cerevisiae. *Genetics.* 111:715–734.

58. Saunders, W., D. Hornack, V. Lengyel, and C. C. Deng. 1997. The Saccharomyces cerevisiae kinesin-related motor Kar3p acts at preanaphase spindle poles to limit the number and length of cytoplasmic microtubules. *J. Cell Biol.* 137:417–431.

59. Machin, N. A., J. M. Lee, K. Chamany, and G. Barnes. 1996. Dosage suppressors of a benomyl-dependent tubulin mutant: evidence for a link between microtubule stability and cellular metabolism. *Genetics.* 144:1363–1373.

60. Carminati, J. L., and T. Stearns. 1997. Microtubules orient the mitotic spindle in yeast through dynein-dependent interactions with the cell cortex. *J. Cell Biol.* 138:629–641.

61. Gupta, M. L., C. J. Bode, D. A. Thrower, C. G. Pearson, K. A. Suprenant, K. S. Bloom, and R. H. Himes. 2002. beta-Tubulin C354 mutations that severely decrease microtubule dynamics do not prevent nuclear migration in yeast. *Mol. Biol. Cell.* 13:2919–2932.